Fracture of Antarctic ice shelves and implications for the icy satellites of the outer solar system

by

Catherine Colello Walker

A dissertation submitted in partial fulfillment
of the requirements for the degree of
Doctor of Philosophy
(Atmospheric, Oceanic and Space Sciences)
in The University of Michigan
2013

Doctoral Committee:

Assistant Professor Jeremy N. Bassis, Chair
Assistant Professor Eric A. Hetland
Associate Professor Michael W. Liemohn
Emeritus Professor Andrew F. Nagy

The moment you doubt whether you can fly, you cease for ever to be able to do it.

– J. M. Barrie, *Peter Pan*

Exploration is really the essence of the human spirit. – Frank Borman

For my family. Together, we'll never stop exploring.

ACKNOWLEDGEMENTS

This writing business. Pencils and what-not. Over-rated, if you ask me. Silly stuff. Nothing in it.

– Eeyore

"I sometimes catch myself looking up at the Moon, remembering the changes of fortune in our long voyage, thinking of the thousands of people who worked to bring the three of us home. I look up at the Moon and wonder, when will we be going back, and who will that be?" Every successful personal essay I have ever written has begun with this quote, and so I figure, why stop now? I blame my entire life's journey thus far on this final quote from *Apollo 13*. Perhaps I am so attached to it because when I heard it when I was 10, I knew I wanted to fly in space and for the last 18 years I've remained convinced that it would be me that would go. It is this attachment to a simple quote that has propelled me—at times, blindly—through the course of my career so far. If over the course of said career I have seemed fantastical, delightfully (or pitifully?) unaware of my own inabilities, or blissfully ignorant of the warning signs of failure in my pursuit - then the folks who observed these behaviors may have been correct. Regardless, at this final point, although nearly every shred of confidence that I've ever had in myself has been torn away in this experience over the last 5 years, there's a final tiny, tiny piece that remains. And the tiny tiny shred repeats the quote. So I stick with it.

A Ph.D. seems like a crown that super-smart people wear, and if anything by the end of this I am absolutely convinced I've only gotten dumber and older, and I convinced that this PhD is the result not of actual brain power, but shear stubbornness and the aforementioned delusions of grandeur. In fact, lyrics from a favorite song by Kansas sums it up best, "Masquerading as a man with a reason; My charade is the event of the season; And if I claim to be a wise man, well, it surely means that I don't know."

That being said, there are quite a few well-intentioned people that helped me get to this pinnacle of bewilderment. First, the fact that I even came to Michigan, even after I had turned it down the first time around, is all thanks to Mike Liemohn. For some reason, he gave me a second chance, and for that I will always be grateful. It turned out pretty well. Secondly, to Jeremy, who agreed to adopt me as a student even though I was already two years in and sort of aimlessly lost. He allowed me to do a lot of what I wanted to do (with lots of guidance along the way), something that was far more enriching than one would think. It's worked out well, my 10-year-old self would be so excited about the things I get to work on - and I've learned to cut down on run-on sentences in the meantime (though that might not be evident here). Thanks to the other two members of my committee - Dr. Nagy and Dr. Hetland - for agreeing to subject themselves to my writing. Thank you to Dr. Nagy for taking an interest in my future throughout my time here. And to Dr. Hetland, I'm sorry I dropped his class a few years ago - aside from Jeremy's ice sheets course, it was the one that might have actually been relevant to my research in geophysics. Also, from my time in the M.Eng. program, thanks to Darren McKague for giving me a vote of confidence even when I was lacking one for myself in my first year in AOSS.

To the friends I've made during my time as a graduate student at Michigan: Shannon, the Sandy Lyle to my Reuben Feffer (or vice versa?); Fang and Matt, my first two officemates; Rona, Xing, and Zhenguang, who let me study for the

space quals with them and are always so friendly; Ahmed, Kristen, Kevin, Paul, Dan, Jacob, Gina, Rachael, Amanda, John - all of whom have supplied humor and smiles (and thankfully, not too many hugs). While my quietness probably sent the opposite message, getting to know you all made my time at Michigan much more pleasant. Among other folks that I should thank here in AOSS are Barb Lupi, who was always pleasant and happy to help (even when she was busy). Sandee Hicks, Marie McKnight, and Margaret Reid, all of whom at different points had to deal with my complaints about being forgotten from the list of current students every semester - I thank them for helping fix things each time even though they likely cringed and heard the "Jaws" theme music each time my name popped into their inboxes. Thanks to Sandra Pytlinski for helping me out over the years even when I wasn't in her charge. Despite not knowing some in the building as well as others, thanks in general to the department for being a fairly friendly place, and to most people for returning smiles in the hallways.

Thanks to my friends from back home, Kelly, Lindsay, and Alicia, who stuck around as friends even though they were not legally required to do so (I'll never understand it). I am convinced that our un-popularity (and only becoming aware of that fact in hindsight) got us through public school happy and in one piece. Thanks to Marissa, my Mount Holyoke partner in crime (and when I say partner in crime, I mean the worst "crime" we attempted was scaling the dorm building to retrieve our paper airplanes) for always being more excited about my life than I was. Thanks to my NASA Academy pals and my UNH comrades for sharing in my excitement about space travel. Thanks to my aunts, uncles, and cousins for providing a supposedly laid-back but actually intensely driven family life. To Grammy and Nonno, Nana and Grandpa, and Margot and Donnie - I wish you were still here.

Weird as it seems, thanks to my trusty purple PT Cruiser - that might sound lame but she's been with me from beginning to end, from Maine to Florida to Maryland to

Michigan, and I don't blame her for being a lemon. I blame Michigan's roads. Thanks to my pets Mojave and JamesWebb - even though you were nocturnal and kept me up at night, I was much less lonely during my first years here in Michigan. Thanks to Sid for the cheesy pick up lines and actually thinking they were funny. They absolutely weren't, but thanks to general confusion it worked out in the end. Thanks to my brother-in-law for still thinking I'm smart, and being Good Old Dave Armstrong even when I'm at my most unpleasant (which is most of the time). Lastly, my family (the people legally bound to deal with me the longest), who unquestionably believe I'll achieve my dream, and have confidence in me regardless of whether I have any in myself. I miss you all the time but it's you who set me on this path, so I will follow wherever it leads and remember that we're all under the same big sky, "somewhere out there". My parents spent their lives helping others as a surgeon and an educator, and the world is a better place for their hard, honest work and dedication. Thanks for letting us chase our own dreams and teaching us that failure only comes when you stop trying. To my dad, who reminds me that it's ok to be "JJ", sometimes "I don't do esophagial work" is the only right answer, and among other things, let us watch Magnum PI when my mom was away - thanks for always being up for adventure. To my mom, who for some reason still holds onto the Pollyana belief that everything works out in the end, sets an inspiring (and sometimes difficult to adopt) example, and when things really do work out, she can use her favorite Kanye West quote, "Don't act like I never told you" - thanks for always laughing. To my sister Cynthia, who is much smarter than me but always gets much less credit, I don't think I'd have a life without her, so it's not really worth saying much else. As we say from Love Actually, "It's a terrible, terrible mistake, chubs, that you turn out to be the love of my life...". And to Enzo, Pasta, Dino, and Rocco, thanks for always being happy to see me (or barking at potential invaders).

TABLE OF CONTENTS

DEDICATION ii

ACKNOWLEDGEMENTS iii

LIST OF FIGURES xi

LIST OF APPENDICES xxii

ABSTRACT xxiii

CHAPTER

I. Introduction 1

1.1 Motivation 1
1.1.1 Evolution of the Antarctic Ice Sheet 2
1.1.2 The Evolution of Planetary Bodies 2
1.2 Geological and Geophysical Settings 3
1.2.1 Earth: Antarctica 3
1.2.2 The Outer Solar System: Icy Moons 7
1.3 Planetary Tectonics 20
1.4 Comparative Planetology 22
1.5 Objectives: Questions Addressed in this Dissertation 24
1.6 Dissertation Overview 25

II. Theoretical Background: Deformation and Fracture of Ice . 30

2.1 Rheology of Ice 30
2.1.1 Planetary perspective: Consideration of ice as planetary bedrock 31
2.2 Linear Elastic Fracture Mechanics 31
2.3 Viscous behavior of ice 34
2.3.1 Viscous behavior in terrestrial ice 34
2.3.2 Viscous behavior in planetary ice 35

2.4 Rheological implications at the icy satellites 37

III. The role of structural and environmental triggers inferred from an Antarctic-wide survey of ice shelf rift propagation . 39

3.1 Introduction 39
3.2 Data and Methods 41
3.2.1 Satellite imagery and image processing 41
3.2.2 Rift length measurement 42
3.3 Results 44
3.3.1 Propagation patterns 44
3.3.2 Temporal patterns of rift propagation 46
3.4 Discussion 46
3.4.1 Role of environmental forcing 48
3.4.2 Role of mechanical forcing controls on rift propagation 51
3.5 Conclusions 54
3.6 Supplementary Figures 55

IV. Variability in Rift Propagation in the Amery Ice Shelf, East Antarctica 66

4.1 Introduction 66
4.2 The Amery Ice Shelf 68
4.3 Data and Methods 70
4.3.1 Satellite imagery 70
4.3.2 Image processing and analysis 70
4.4 Results 71
4.4.1 Average rift propagation rates 71
4.4.2 Seasonal variability 73
4.4.3 Evidence for linked activity between rifts 73
4.4.4 Large propagation events 77
4.4.5 Atmosphere and ocean forcing 78
4.5 Discussion 80
4.6 Conclusions 82

V. Propagation of Closely-spaced Fractures in a Planetary Ice Shell 84

5.1 Introduction 84
5.2 Crack propagation model 87
5.2.1 Stress intensity due to tensile stress 88
5.2.2 Stress intensity due to overburden stress 88
5.2.3 Stress intensity modification by multiple fractures . 90
5.2.4 Bottom cracks 91
5.3 Model parameters and experimental setup 93

5.4 Results . . . 93
5.5 Discussion . . . 95
5.6 Conclusions . . . 97

VI. On the Formation of a Rift Basin in the Ice Shell at the South Pole of Enceladus . . . 98

6.1 Introduction . . . 98
6.2 On the North Fiji Basin . . . 101
6.3 Mechanical models of basin formation . . . 104
6.3.1 An icy analog: Enceladus' structure . . . 104
6.3.2 Subsidence of the SPT floor . . . 108
6.4 Model results and comparison to topographic observations . . . 115
6.4.1 Subsidence of the basin floor due to thinning . . . 115
6.4.2 Flexural response of the crust . . . 115
6.5 Discussion . . . 119
6.5.1 Thinning and flexural uplift: Integrated model . . . 119
6.5.2 Terrestrial basins and implications for the SPT . . . 123
6.6 Conclusions . . . 125

VII. Conclusions and Future Work . . . 126

7.1 Summary . . . 126
7.2 Contributions . . . 128
7.3 Future Work . . . 131

APPENDICES . . . 135
A.1 The flexural model in a spherical shell . . . 136
A.1.1 Flexural formulation . . . 136
A.1.2 Comparison of spherical shell flexure to Cartesian geometry . . . 140
A.2 Effects of bending moment and membrane forces on stress intensity factors in spherical ice shells . . . 141
B.1 Introduction . . . 145
B.2 Experimental regimes of crustal deformation . . . 146
C.1 Introduction . . . 150
C.2 Theoretical Background . . . 151
C.3 Laboratory Background . . . 152
C.4 Theoretical Approach . . . 153
C.4.1 Principles of the Experiments . . . 153
C.4.2 The Andrade Model . . . 154
C.5 Experimental Approach and Methodology . . . 156
C.5.1 Physical Constraints . . . 158
C.5.2 Ice Factory Setup . . . 160
C.5.3 Compaction . . . 162

C.5.4 Tidal Stress Simulation Facility 162
C.6 Data Analysis 164
C.7 Results 165
C.7.1 Experimentally-derived viscosity 165
C.7.2 Grain size: Expected vs. actual 166
C.7.3 Microstructure 166
C.7.4 Data-model comparison: The Andrade Model 168
C.8 Summary of Conclusions and Future Work 171
C.8.1 Conclusions 171
C.8.2 Future work 172

BIBLIOGRAPHY 173

LIST OF FIGURES

Figure

1.1 A cartoon showing the primary mass gain and loss mechanisms for the Antarctic Ice Sheet and its associated ice shelves. The ice sheet gains mass through accumulation of snow. It loses mass through two main mechanisms: basal melting and iceberg calving and at a smaller rate, through surface ablation (sublimation, melt, evaporation). . . . 5

1.2 A map of Antarctica shows a sampling of the larger ice shelves that surround the continent. Base image is the Landsat 7 Image Mosaic of Antarctica (LIMA). The largest are the Filchner-Ronne, Ross, Amery, and Larsen C ice shelves. Ice shelves can be embayed (e.g., Ross, Amery) or more freely-spreading, set among pinning features (e.g., Abbott, West, and Shackleton ice shelves). 6

1.3 Series of images shows the initiation, propagation, and calving of an iceberg from the Pine Island Glacier in 2001. (a) a transverse-to-flow rift initiated from an array of cracks at the embayment wall; (b) 14 months later, the rift has propagated across about 3/4 of the ice shelf at a rate of approximately 15 m day^{-1}; (c) the rift ultimately propagates across the last 1/4 of the ice shelf's width between 4 November and 12 November of 2001, isolating an iceberg (42 $\times$17 km) that was then free to drift away. Representative of calving cycle observed there, as a similar series of events occurred in 2007, and again in late 2011 (it has propagated to within meters of severing the entire shelf width as of March 2013). This demonstrates that propagating rifts serve as the border for future icebergs as they approach the front. Image credit: NASA/GSFC/LaRC/JPL, MISR Team. 8

1.4 Various appearances of mountainous ridge features at icy moons. (a) "grooved terrain" at Ganymede; (b) ridges cross-cutting other fractures at Europa; (c) parallel mountain chains northwest of Xanadu on Titan; (d) compression folds in Enceladus' Northern hemisphere; (e) grooved terrain on Miranda. Image(s) credit: NASA/JPL/Space Science Institute 10

1.5 Enceladus' size compared to the familiar shape of the United Kingdom. It is Saturn's sixth-largest moon, and has a diameter of 505 km. Image courtesy: Image courtesy NASA/JPL/Space Science Institute. 11

1.6 A global basemap mosaic of Enceladus created by NASA / Jet Propulsion Lab / Space Science Institute shows the variety of tectonized terrains on the small moon. Developed with images captured during the October and November 2009 Cassini flybys, July 2006 flybys, and the Voyager 2 flyby in 1981. 13

1.7 The trailing hemisphere of Enceladus showcases the Cufa Dorsa region (left) and Labtayt Sulci (right), which stems from the South Polar Terrain (upper right, middle image). Cufa dorsa features ridges thought to be the result of compressional tectonics, while Labtayt Sulci is a deep canyon hypothesized to be the result of extensional tectonics associated with the formation of the SPT. These images were captured October 5, 2008 during a flyby that took Cassini within 15 km of the surface. Image Credit: NASA/JPL/Space Science Institute 14

1.8 Enceladus vents subsurface materials into space. Top: The south pole of Enceladus, imaged during the 2009 flybys of Cassini. The four prominent tiger stripe fractures at the center are surrounded by a near-circular boundary of mountainous uplift. The entire region is depressed into the surface by 200-800 m. Middle left: A raw image captured on approach by Cassini shows the Sun-illuminated geysers from the south pole. Middle right: Enceladus' south polar vents release water and gas and supplies the E-ring of Saturn. Bottom: A close-up view captured in May 2012 of the jets set along the tiger stripe fractures themselves; one of the last images to be captured of the south pole of Enceladus by Cassini prior to this region going into shadow for the years to come. Image Credit: NASA/JPL/Space Science Institute 16

1.9 Patterns of fracturing cover Europa. Reddish linear to curvilinear features are observed - the reddish-brown material is a non-ice contaminant that colors Europa's frozen surface, likely from subsurface interaction or impactor contamination of the surface. Data used to create this view were acquired by the Galileo spacecraft in 1995 and 1998. Right image shows an example of the "chaos terrain" called Thera Macula. This terrain is found distributed over Europa's surface. Image credit: NASA/JPL/Ted Stryk 18

1.10 False-color image of Europa's highly fractured and ridged surface. The complicated chronology mapping of ridges and cracks points to considerable geological activity. Mosaic created by images captured by the Galileo spacecraft. Image credit: NASA/JPL 20

2.1 Three modes of fracture: (a) Mode I fracture: tension normal to the fracture plane. (b) Mode II fracture: sliding mode due to shear loading. (c) Mode III fracture: tearing mode due to out-of-plane shear loading. 32

3.1 Image enhancement and methods of measuring rift length for different rift orientations. (a) Raw MODIS image of the Amery Ice Shelf from 11 February 2012. (b) Brightened and contrast-stretched version of same MODIS image. (c) Red circles denote beginning and end points for measuring rifts. Shown here is a front-initiated rift (left) and a rift initiated from a triple junction (right). Red lines denote the measured length. (d) The Fimbul Ice Shelf in a contrast-enhanced MODIS image from February 2012. Inset: Red circles denote beginning and end points of measurement for a double-ended rift. 43

3.2 Ice shelf locations and categories of rift propagation observed. Each block denotes a rift and the color of the block denotes the type of rift activity observed (see legend). 45

3.3 Each panel shows atmospheric temperature, the monthly range of sea ice concentration from maxima and minima and rift propagation rates for each ice shelf. Top: Monthly mean temperatures for each ice shelf over the decade, from ERA interim reanalysis data. Middle: Gray shaded regions are maximum and minimum annual sea ice extents in front of each ice shelf from passive microwave measurements. Bottom: The length of each bar represents the annual propagation rate with bars color coded to label the different rifts in ice shelves (supplementary Figs. S1-S10). White arrows signify rifts with two actively propagating rift tips. White diamonds signify calving events. White zig-zag signifies rifts propagating in a crevasse field. Left-triangles signify a collapse event. 47

3.4 Examples of rifts that exhibited propagation events following the arrival of a tsunami. Each block indicates a rift that propagated following the arrival of a tsunami. The color of the block denotes whether the rift propagation event was also associated with an iceberg calving event. Rift propagation was observed in the rifts that are exposed to the specific wave path of a given tsunami. Wave paths associated with tsunamis that originated near Sumatra, Chile and Japan are sketched schematically (NOAA Center for Tsunami Research). . . . 52

3.5 MODIS imagery from 20 December 2011 of the Amery Ice Shelf, East Antarctica (left). Zoomed views of the five rifts monitored in this study (boxes, right), color coded by activity level (legend in Fig. 1). 55

3.6 MODIS imagery of the Fimbul Ice Shelf acquired 28 November 2005 (top). Zoomed boxes (bottom) show the 11 rifts observed for this study. Rift F3 calved an iceberg prior to this study's observation period, but served as an initiation boundary for F3a and F3b. . . . 56

3.7 Filchner Ice Shelf (left) as imaged by MODIS acquired 13 February 2011 (left). Zoomed boxes (right) showing the six rifts observed for this study in MODIS imagery acquired 02 January 2003. 57

3.8 The Ronne Ice Shelf in MODIS imagery acquired 01 December 2007 (left). Zoomed boxes highlight the seven rifts observed in this study. 58

3.9 MODIS imagery from 17 March 2002 of the Larsen C Ice Shelf and remnant Larsen B Ice Shelf on the Antarctic Peninsula (right). Zoomed images of its northern rifts shown in the center column. To the right are the southern set of rifts observed in this study, a total of 11 rifts on this ice shelf. 59

3.10 MODIS imagery from 30 December 2004 of the Wilkins, Stange, and George VI ice shelves on the Antarctic Peninsula. Zoomed images on the right exhibit the rifts observed for this study in each of the three shelves: (1) Wilkins Ice Shelf, (2) Stange Ice Shelf, and (3) George VI Ice Shelf. 60

3.11 Abbott Ice Shelf in MODIS imagery acquired on 10 January 2011. Zoomed boxes (bottom) show the seven rifts observed for this study. 61

3.12 Ross Ice Shelf in MODIS imagery acquired on 16 November 2011 (top). At the bottom are zoomed images to highlight the ten rifts observed in this investigation. 62

3.13 The Shackleton Ice Shelf in MODIS imagery from 20 February 2012 (right). On the left is a zoomed view of the two rifts measured in this study, stemming from a previously-calved area that spurned an iceberg immediately preceding the observing period. 62

3.14 West Ice Shelf in MODIS imagery from 06 February 2004 (left). The center blocks highlight the western set of rifts observed for our study, the eastern set is shown in the zoomed images at right. Initially observing just seven rifts on the Shackleton, rift BB2 (top center) split into two new rifts (BB2a and BB2b) that we continued to observe over the decade. 63

3.15 Two MODIS images of Pine Island Glacier acquired five years apart. Top: An image from 19 March 2007 shows rift PIa, which calved an iceberg in October 2007. Bottom: An image from 01 January 2012, showing that rift PIb has severed the ice approximately three-quarters across the glacier. 64

3.16 An example of wintertime propagation exhibited by rift WR6 in the Ross Ice Shelf between 13 March and 15 October 2009. Vertical dashed lines show length of rift in March 2009 (top), bottom image shows the same rift in October 2009, where it has lengthened past the length of the rift before the winter. 65

4.1 False-color MISR (Multi-angle Imaging SpectroRadiometer) images acquired 07 January 2010 show the full Amery Ice Shelf (a) and a zoomed-view of the ice shelf front (b). The five rifts monitored in this study are labeled in black (white trace). (c) A zoomed view of rift T1 acquired 27 January 2012 shows its changing propagation direction as it crosses a suture zone in the ice shelf. (d) A zoomed view of rift E3 acquired 17 November 2002 shows its meandering path among pre-existing crevasses near the ice front. 69

4.2 The Amery's front positions from Fricker et al. (2002) from 1963 and 1965, framing the last major calving event of the Amery in late 1963/early 1964, are juxtaposed onto a MISR image showing its current front position. 69

4.3 The relative change in length for each rift illustrates the general trend that all rifts lengthened over the decade. Gray regions indicate the seasons observed, and dotted lines highlight decadal averages for rift propagation (shown at right). Rift positions are shown (map, inset). 72

4.4 Panels (a) through (e) show change in rift length per season. Length changes over the winter are calculated relative to the length at the end of the previous season. Vertical lines in matching color mark propagation events that are outside of the inter-quartile range of the data. Black lines show average propagation rate per season. Panel (f) shows sea ice concentration (blue) and yearly sea ice maxima and minima (red) in front of the Amery; orange lines denote months in which average atmospheric temperature surpassed 0 °C as measured from Mawson and Davis stations. Dotted gray vertical lines denote occurrences of Indian Ocean tsunamis that reached the Amery over the decade. 74

4.5 The correlation of movement between specified rift pairs shows whether pairs propagate in tandem or are offset from each other. The left panel shows relationships between the pairs between 2002-2006; the right panel shows the altered relationships between rift pairs in the years following the initiation of W1 in 2006. The center panel shows the combined correlation coefficients over the decade. 76

5.1 Free-body diagram of multiple cracks in a region of ice. σ_O is the overburden stress which increases with depth. σ_T is the tensile stress acting on the brittle layer of thickness H, initiating cracks of depth d, which are spaced 2W apart. 90

5.2 Fractional penetration depth (d/H) of surface fractures for a range of tensile stress (0.2-3 MPa) in a 30 km Enceladus shell (left) and a 1 km Europa shell (right). Blue markers signify d/H for a single fracture, green markers signify d/H for a fracture in a fracture array. 94

5.3 Fractional penetration depth (d/H) of basal fractures for a range of tensile stress (0.2-3 MPa) in a 30 km Enceladus shell (left) and a 1 km Europa shell (right). Blue markers signify d/H for a single fracture, green markers signify d/H for a fracture in a fracture array. 95

6.1 Enceladus' South Polar Terrain, imaged by Cassini (NASA/ JPL/ Space Science Institute). The major sections of topography at the SPT are denoted here: the four main tiger stripes marked in red, within the central depressed tiger stripe terrain outlined in yellow; the surrounding region that appears mottled but has few fractures itself, also depressed, outlined in green; the green outline, thereby, also highlights the location of the mountainous uplift at the boundary of the region. The highest point of uplift is estimated at 1 km. Blue lines radially outward from the SPT mark two of the "starfish arms" - large-scale fracture features radiating away from the SPT towards the equator. 100

6.2 A tectonic map of the North Fiji Basin in the South Pacific ocean. The multiple active parallel rifts at the center region of the basin lie in a region that is depressed by about 500 m. They are surrounded by a convergent zone to the south, east, and west and a remnant rift to the north. 103

6.3 Schematics of the three basin models considered: (a) Thinning model: a section of crust is stretched by β, thereby thinning the solid layer by β, which leads isostatic imbalance and subsequent subsidence at the surface. (b) Extensional model of rift flank uplift: Dependent upon elastic response in the crust, we envision tensional forces pull apart a crustal block which breaks at angle θ_b, causing uplift u_r. The footwall block (right) rises to maintain isostasy above the hanging wall block (left). (c) Compressional model of rift flank uplift: assuming an elastic response in the crust, we envision that horizontal forces push on a block until it breaks, causing a reverse fault and uplift u_r. All three models are dependent on layer properties, most importantly ρ_i (ice density), and the density of the underlying substratum, ρ_u. In our models we consider several states for ρ_u. 105

6.4 Model structure for Enceladus. We assume an ice shell of thickness 50 km over an ocean of 40 km depth, for a total outer water-ice layer of 90 km. For models of flexure, we assume that the elastic thickness, T_e (light gray), at Enceladus is 1 km. The brittle layer of ice, or the depth t which fractures penetrate (d), is taken to be 3 km (though we experiment with upper bounds in our results). We assume a surface temperature of 70 K, a thermal gradient in the ice layer (thick black line), and an isothermal water ocean (dark gray) beneath at 273 K. 107

6.5 Schematic diagram illustrating the geometry of a section of shell in extension and the effective load neccessary in order to return to isostatic equilibrium after a normal fault disrupts balance. (a) Prior to rifting, extensional stresses act on a section of shell; (b) the right hanging wall block slides downward, creating an isostatic imbalance thereby inducing uplift of the left footwall block; (c) a second break due to bending stress creates (ideally) a symmetric graben structure about the South Pole. Adapted to the spherical equivalent from *Watts* (2001), Figure 7.6. 112

6.6 Flexure of the ice shell due to thinning-induced subsidence (top), used to calculate associated tensional stress (bottom). Black squares in the bottom panel show points at which stress surpasses 1 MPa, our assumed yield strength of ice. These locations are translated to the top plot in white, showing the locations at which the ice will fail, noting that negative stress implies compressive stress. This break allows for uplift at the boundary and shows the width of our predicted basin, roughly 240 to 310 km across, assuming an elastic response in the ice. 116

6.7 Footwall uplift in the case of extensional forces at the boundary of the SPT area. Uplift varies with assumed layer properties. Case A (green): Fracturing penetrates the entire ice thickness ($d = H_i$), and underlying substratum taken to be water ($\rho_u = \rho_w$). Case B (dark blue): Fracturing penetrates an brittle layer of 3 km, over a warm ductile ice layer, whose density is related to the temperature gradient in the ice layer (coldest ice at surface: 933 kg/m^3, warmest ice at base: 917 kg/m^3), i.e., $\rho_u = \rho_{i(warm)}$. Case C (light blue): Fracturing penetrates a brittle layer of 3 km, over a substrate of a "slushy" ice-water mixture. 118

6.8 Footwall uplift profile in the case of compressional forces at the boundary of the SPT area. Case A (dark blue): Fracturing penetrates the entire ice thickness ($d = H_b = H_i$), and underlying substratum taken to be water ($\rho_u = \rho_w$). Case B1 (purple): Fracturing penetrates a brittle layer of 3 km, over a warm ductile ice layer, whose density is related to the temperature gradient in the ice layer (coldest ice at surface: 933 kg/m^3, warmest ice at base: 917 kg/m^3), i.e., $\rho_u = \rho_{i(warm)}$. Case B2 (green): similar to Case B1 in structure, this case was used to illustrate the small effect of assumed substratum density on result. In this case, we assume no density difference between the brittle ice and underlying ice, resulting in only a small change from the density-gradient version in Case B1. Case C (light blue): Fracturing penetrates a brittle layer of 3 km, over a substrate of a "slushy" ice-water mixture. 120

6.9 The topographic profile (black) of the SPT from *Schenk and McKinnon* (2009) is used to illustrate model results. Left hand navy blue line denotes the best-fitting result from the extensional model. This reaches approximately 1.8 km in height, assuming a brittle layer overlying a warm ductile ice layer. On the right hand side, the green line denotes our best fit curve of flank uplift in the compressional model, reaching 1.15 km, assuming a brittle layer of 3 km over a ductile layer of ice beneath. This result and structure match previous estimates of elevation and internal structure. Purple line denotes the subsidence we find from our thinning model (600 m depression); we put this in context of previous estimates of the depression depth at the SPT (*Thomas et al.* (2007) and *Roberts and Nimmo* (2008) (red); *Helfenstein et al.* (2011) (yellow); *Schenk and McKinnon* (2009) (green (lowest estimate)); teal box denotes the span of estimated depths at the South Pole). Due to the uncertainty in parameters at Enceladus, we include error in our assessment, marked by the gray box. Maximum extensional stress (magenta) and compressional stress (orange) are marked by boxes (see Fig. 6.6). Note that the profile is a single side of the basin mirrored over the central axis. 122

B.1 A preliminary study: formation of mountainous ridges at Enceladus by basal flow into a backstop. Formation of desired topography (uplifted side walls and depressed center) and thinned region at center matches well with expected setting at the SPT. 148

B.2 A preliminary study: formation of mountainous ridges at Enceladus by collision of moving backstop and stationary ice (approximating far-field compressional tectonics). Formation of uplifted side walls and some depression at the center. Hill buildup at center is a remnant of our model geometry. 148

B.3 Preliminary model application at Enceladus shows development of surface depression and mountainous ridges when extensional forces are applied to a thin brittle layer. Red symbolizes broken bonds, dependent on set ice strength. Inset (bottom) shows fractured ice in depressed region over localized ocean (zoomed view). 149

C.1 Coefficient of friction (equivalent to the inverse of the dissipation factor) in ice as a function of frequency. This example employs an assumed grain size of 100 μm and a temperature of 240 K to show the difference in phase lag response predicted by the Maxwell model (blue) and the Andrade model (red). Note the change in frequency dependence between the models and the "elbow" behavior predicted by the Andrade model. 155

C.2 Phase lag ($\sin\delta$) as a function of frequency according to the Andrade model. Viscous properties are dominant at low frequencies; anelastic properties become dominant at high frequencies. Note changing slope of the curve, characteristic of the Andrade attenuation spectrum. . . 157

C.3 Phase lag as a function of temperature and frequency as predicted by the Andrade approach. Red color indicates a larger phase lag, while bluer color represents smaller phase lag. Though similar in appearance, a noticeable difference here is the larger range of phase lag achievable in the dislocation creep regime (10^{-7} up to 10^{2}). . . . 157

C.4 Phase lag as a function of temperature and frequency as predicted by the Andrade approach. Red color indicates a larger phase lag, while bluer color represents smaller phase lag. Though similar in appearance, a noticeable difference here is the larger range of phase lag achievable in the grain boundary sliding regime (10^{-6} up to 10^{1}). 158

C.5 Deformation map: Solid lines delimit conditions that promote various creep regimes. Dotted lines correspond to the conditions of tidal stress and temperature relevant to various icy moons in the solar system. This plot was obtained assuming a uniform grain size of 500 μm, and an assumed temperature of either the moon's surface temperature or, in the case of moons known to employ convection in their shells, a temperature of 200 K. Additionally, calculated tidal stress values based on orbital eccentricity were used to demonstrate the regime(s) that is likely occurring in each moon of interest. . . . 159

C.6 Grain size determination: To determine which grain size to use for our sample, we used models like this one and constrained the possibilities to be between 235 and 245 K, and between 0.2 and 0.6 MPa. In limiting the grain size to be under 500 μm, we determined that 300 μm would work best, though such large sizes had not been tested in the lab before. 161

C.7 A photo of the Instron system, in which the cylindrical ice sample is placed and tested through cyclical stresses from the top platen (this particular test concerned a clathrate sample). 163

C.8 A photo of the Instron system, in which the cylindrical ice sample is placed and tested through cyclical stresses from the top platen (this particular test concerned a clathrate sample). 164

C.9 Various captures taken by the cryo-microscope of the ice sample after compaction but prior to insertion into the Instron instrument. Lack of porosity and different grain sizes are observed. The sample featured an average grain size of 150 μm, +/- 50 μm. Figs. a-c were taken using a polarized light source and color represents changes in material. Figure (d) shows the same section as in (c) using reflected light. Notable here are the formation of small cracks (or sub-grain boundaries) in some of the larger grains (e.g., large grain at bottom left) 167

C.10 Images of the post-Instron sample. Air bubbles are a product of melting that occurred during transport between the storage freezer and the cryo-stage. Images are composites of many focused images, as the sample had varying thickness across it. Some sub-grain boundaries can be observed in the larger grains, for example in the large grain at the top-left of (a), and the enlarged view of a grain featuring a sub-grain boundary formation in (c). Noticeable in all three images is the lack of porosity between grains, and for the most part, similar grain sizes as the pre-Instron images. These observations are consistent with past data sets. 169

C.11 Best fit of the Andrade model (red) to laboratory data collected in July-August 2010 (blue/green). Consistent with past data sets, it fits the data well at both high- and low-frequency. The Maxwell model (purple) does not fit the data as well as the Andrade curve, showing that our laboratory data supports the Andrade model. 170

LIST OF APPENDICES

Appendix

A. Consideration of the Spherical Shell in Tectonic Problems 136

B. Bounds on Compressional Features in the Ice Shell of Enceladus . . . 145

C. Laboratory Observations of Water Ice: Effect of Microstructure and Deformation Regimes on Anelasticity of Water Ice - Implications for Europa, Enceladus, and Titan 150

ABSTRACT

Fracture of Antarctic ice shelves and implications for the icy satellites of the outer solar system

by

Catherine Colello Walker

Chair: Jeremy N. Bassis

Recent observations have revealed that many icy satellites of the outer solar system either are–or were geologically recently–active, evidenced by highly-fractured surfaces and eruption-modified landscapes. It is likely that this activity results from tidal and tectonic stresses throughout their evolution. While it is not feasible at current to study these satellites through fieldwork or even extended remote sensing campaigns, it is possible to study possibly analogous features on Earth to constrain models and improve understanding of fracturing processes that may have occurred there. Morphologically similar to fracture systems observed in the icy moons, large rift systems propagate in terrestrial ice shelves, floating extensions of ice sheets over water. This dissertation presents results from observations of ice shelf rift propagation, and the use of these results in a comparative study of deformation and fracturing in the icy moons. In observing 78 ice shelf rifts around the Antarctic Ice Sheet, we found that variability in rift behavior could not be explained by changing environmental conditions that had previously been suggested to modulate rift propagation, like atmospheric temperature and ocean swell. Instead, we found variability can likely be

attributed to structural heterogeneity within the ice and rift location and geometry, in that we found that open-ended rifts adjacent to the ocean at ice shelf fronts were susceptible to tsunamis. We also found that closely-spaced rifts' behavior was affected by interaction. Motivated by this observation, we showed that closely-spaced surface fractures in the icy moons cannot fully penetrate the shell thicknesses previously predicted. Instead, we argue that a combination of surface and bottom cracks and shear failure must exist for a fracture to reach a subsurface reservoir. We also argue that the bizarre set of features at Enceladus' south pole may be the result of localized thinning, which caused extensional and compressional fracture formation at that location, a phenomenon also seen on Earth. The work presented demonstrates the advantages of comparative study, as we develop an improved set of observations for Antarctic ice shelf rift propagation and use those results to advance the current state of knowledge of planetary properties and processes.

CHAPTER I

Introduction

"Begin at the beginning," said the King, "and go on 'til you come to the end; then stop." – Alice's Adventures in Wonderland

1.1 Motivation

The fracture of ice and snowpack is a familiar concept, for example, to those questioning the safety of a wintertime ice-skating pond, or to skiers pondering the imminence of an avalanche in the area. The phenomenon can be observed on a larger scale, too, where it contributes to the dynamics of glaciers, ice sheets, ice shelves, and even planets. The study of the evolution of ice sheets and glaciers on the Earth, a discipline called glaciology, has come increasingly into focus in recent years as awareness of global climate change has intensified. While ice is readily available to the everyday observer on the ice rink or in an ice cube, larger scale processes behind the dynamics of ice sheets and shelves remain elusive. The focus of this dissertation is on the dynamics of ice and how it fractures. In particular, this dissertation focuses on the role of fracturing in Earth's polar region and the formation of mysterious features on the icy moons of the outer solar system.

1.1.1 Evolution of the Antarctic Ice Sheet

Sea level rise is of particular interest not only to the climate change research community, but also those who live on coastlines worldwide. Future sea level rise is attributed to the loss of mass from Earth's ice sheets and glaciers. The Antarctic Ice Sheet is the largest ice mass on the planet. As the Antarctic Ice Sheet flows outward towards the continental margin, the ice eventually detaches from the ground and transitions to floating ice (Fig. 1.1). Occasionally, sections of ice break off from the ice shelf, in a process called "calving". Iceberg calving accounts for up to half of the total ice discharged from the Antarctic Ice Sheet to the ocean, with basal melting accounting for the remainder, though these proportions vary between different ice shelves (*Rignot and Jacobs*, 2002; *Rignot and Thomas*, 2002; *Rignot*, 2006). Despite this fact, the iceberg calving process remains poorly understood and thereby is not well encapsulated by models of ice sheet dynamics and mass balance. Although iceberg calving itself does not directly affect sea level rise (since the ice is already afloat), ice shelves have been hypothesized to have a buttressing effect on the Antarctic Ice Shelf, preventing acceleration of grounded ice (e.g. *Rignot et al.*, 2004; *Joughin and Alley*, 2011).

1.1.2 The Evolution of Planetary Bodies

The study of the icy satellites is important because it will allow us to better understand how these bodies formed, how they evolved over time, why their appearances vary so widely, and address questions of astrobiological potential, a topic at the forefront of the search for life in the universe. Many planetary bodies can be observed by telescope only, and often the only evidence available study surface and sub-surface processes is satellite imagery. Since it is difficult to travel to these bodies to conduct any kind of field work, we use Earth analogues to better understand processes that could be occurring at these planets and moons. Specifically, the fracture of the ice

that makes up the shells of many satellites is an important process to understand. Assessment of fracture depth and opening rates of cracks can constrain shell thickness over putative subsurface reservoirs, which can also constrain sub-surface heat. Observable surface fracture patterns also constrain orbital characteristics and trace changes over time, both of which contribute to an understanding of planetary evolution since formation. Orbital history and ice shell thickness are also important to the astrobiological potential of these worlds. In addition, our study of the dynamics of planetary surfaces serves as a platform to understand processes active (or previously active) on many of the terrestrial bodies of the solar system and our findings could be easily applied elsewhere, icy or rocky.

1.2 Geological and Geophysical Settings

In our astro-glaciological investigation, we study ice in both the terrestrial setting and in the planetary setting. The main two icy moons studied here are Enceladus, a moon of Saturn, and Europa, a moon of Jupiter. We next describe the physical settings and characteristics of these locations.

1.2.1 Earth: Antarctica

1.2.1.1 The Antarctic Ice Sheet

The Antarctic Ice Sheet contains enough fresh water to raise global sea level by approximately 57 m (*Hooke*, 2005), and one of the biggest questions in Earth science is just how fast this will happen. Current sea level rise is approximately 3.2 mm yr^{-1} (*Rahmstorf et al.*, 2012), a value almost 60% greater than that predicted by the United Nations' Intergovernmental Panel on Climate Change (IPCC). There are a few contributors to sea level rise, the largest of which is thermal expansion of the ocean (1.6 mm yr^{-1}, e.g., *Meehl et al.* (2005)). About a third to one half of sea level

rise is due to the melting of Earth's ice sheets and glaciers (e.g. *Meier*, 1984; *Meehl et al.*, 2005). An increase in the discharge of ice from the ice sheets and glaciers to the oceans due to rising atmospheric and ocean temperatures (either via increased melt rates or iceberg calving) could significantly alter projections of sea level rise in the near future. Approximately half of the world's population lives within 200 km of a coastline, a number which will only increase (e.g. *Hinrichsen*, 1999). Yet, despite the implications of sea level rise on both humans and land use changes, knowledge of the interaction of the climate system and ice dynamics and mass loss remains insufficient to confidently assess changes in ice discharge in the long term (*IPCC*, 2007).

The Antarctic Ice Sheet, like other ice sheets and glaciers, gains mass through accumulation of snow at the surface (*Paterson*, 2000). It loses mass through two main mechanisms: basal melting and iceberg calving (illustrated in Fig. 1.1). At a smaller rate, it can also lose mass by surface ablation (sublimation, melt runoff, evaporation). While basal melting has become easier to quantify, the calving of icebergs from ice shelves remains more difficult to assess. This is mostly due to the fact that iceberg calving events are sporadic and not easy to predict. The removal of large amounts of mass nearly instantaneously via iceberg calving has significant implications for the stability of the ice sheet. Formerly a controversial hypothesis (e.g., *Thomas* (1979) versus *Hindmarsh* (1996)), the ice shelves' potential buttressing effect was showcased following the collapse of two sections of the Larsen Ice Shelf on the Antarctic Peninsula. Following the Larsen A collapse in 1995, *Rott et al.* (2002) observed an up to 3-fold increase in velocity in two of its tributary glaciers. Following the Larsen B collapse in 2002, five glaciers that flow into the collapse area sped up (*Scambos et al.*, 2004; *Rignot et al.*, 2004). During the same period, glaciers south of the collapse zone showed little change.

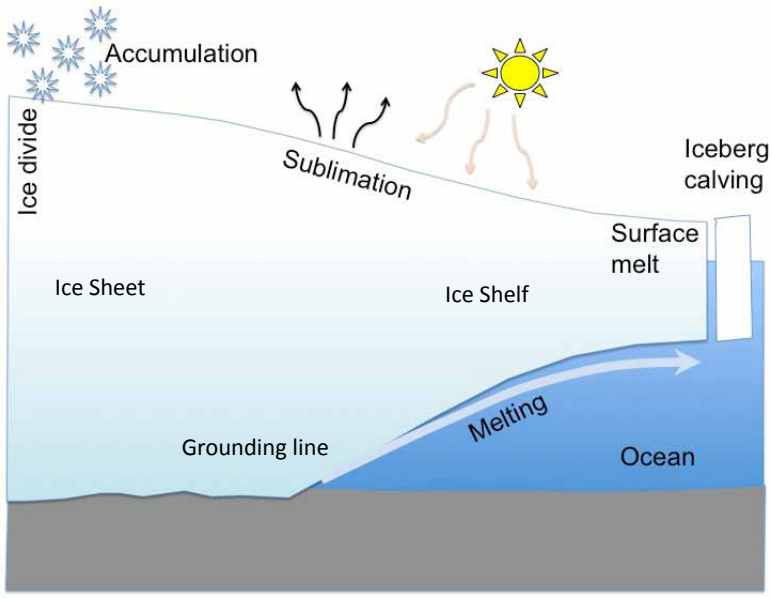

Figure 1.1: A cartoon showing the primary mass gain and loss mechanisms for the Antarctic Ice Sheet and its associated ice shelves. The ice sheet gains mass through accumulation of snow. It loses mass through two main mechanisms: basal melting and iceberg calving and at a smaller rate, through surface ablation (sublimation, melt, evaporation).

1.2.1.2 Antarctic Ice Shelves

Our study focuses on ice shelves, floating platforms of ice that surround the Antarctic coast (Fig. 1.2). They developed and continue to evolve as ice from the Antarctic Ice Sheet flows outward and transitions from a grounded to a floating state (this transitional zone is called the "grounding line"). Ice shelves can range in thickness between thousands of meters at the grounding line to hundreds of meters at the ice front. Resistive stresses from embayment walls and shallow subshelf topography limit the rates at which ice shelves can spread. Since ice shelves are in contact with both the atmosphere and the ocean, they have been hypothesized to be likely sensitive indicators of climate change (e.g. *Doake and Vaughan*, 1991). Since ice shelves are already floating, they do not contribute directly to sea level rise, but their discharge does contribute to the freshwater budget of the Southern Ocean, which may affect temperature and circulation changes. This may occur both through melting

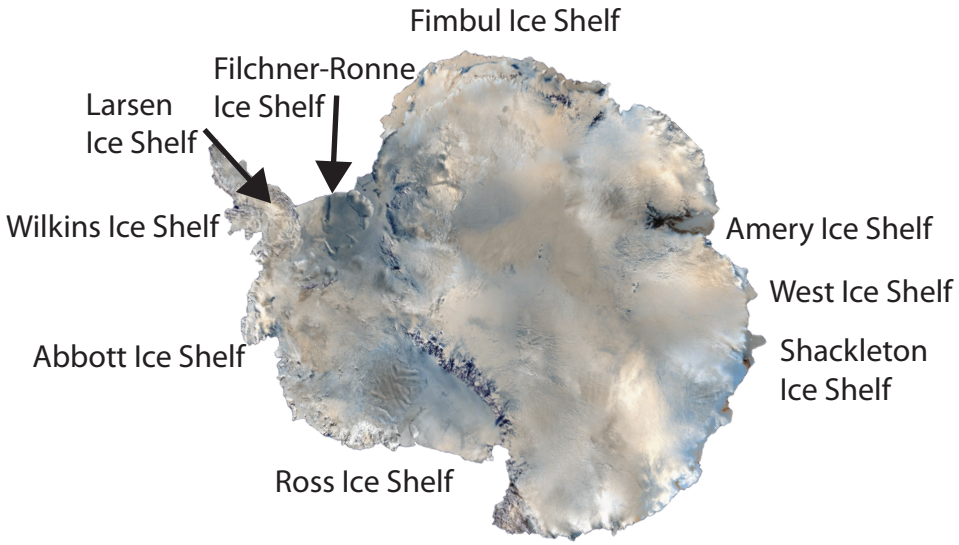

Figure 1.2: A map of Antarctica shows a sampling of the larger ice shelves that surround the continent. Base image is the Landsat 7 Image Mosaic of Antarctica (LIMA). The largest are the Filchner-Ronne, Ross, Amery, and Larsen C ice shelves. Ice shelves can be embayed (e.g., Ross, Amery) or more freely-spreading, set among pinning features (e.g., Abbott, West, and Shackleton ice shelves).

and through the migration of icebergs, which melt as they drift towards mid-latitudes. Additionally, the calving of icebergs from the ice shelves can lead to increased flow of inland grounded ice towards the oceans—which does contribute to sea level rise—through loss of buttressing (e.g. *Joughin and Alley*, 2011; *Pritchard et al.*, 2012).

1.2.1.3 Iceberg Rift Propagation and Iceberg Calving

Direct observation of iceberg calving events are rare. Large iceberg calving events, however, do occur as part of a cycle, in which the ice front advances by ice flow beyond its embayment walls and then retreats by calving. Recurrence intervals for this cycle vary by ice shelf, but are typically on the order of many decades (e.g. *Scambos et al.*, 2003; *Bassis et al.*, 2007). Iceberg calving has also been implicated in some of the most rapidly changing regions of Antarctica. *Scambos et al.* (2003) showed that the abrupt disintegration of both Larsen A and Larsen B ice shelves occurred following a

series of abnormally warm summers. Not only were these disintegrations surprising in terms of size, but also in the speed at which they occurred. The Larsen A Ice Shelf decreased in size over many years before completely collapsing in about one week in 1995; almost all of the Larsen B Ice Shelf collapsed over the course of five weeks in 2002, much faster than predicted even having observed the warning signs (*Scambos et al.*, 2003). The large ice shelves of Antarctica, Ross, Ronne, Filchner, and Amery ice shelves (Fig. 1.2), primarily exist further south (i.e., in colder temperatures) than those on the Antarctic Peninsula and have not experienced comparable surface melting nor are they showing any signs of imminent peninsular-style disintegration.

To better understand iceberg calving, it is useful to observe the initiation and propagation of rifts, the precursor to iceberg calving (Fig. 1.3). Rifts are large fractures that penetrate the entire ice thickness. Icebergs detach when one or more rifts isolate an iceberg that is then free to drift away. Rifts often form upstream of the calving front and can advect for decades or centuries before isolating an iceberg. In other cases, rifts initiate close to the ice front (within tens of kilometers) and propagate for shorter periods of time (years to decades) prior to either becoming inactive or isolating an iceberg.

1.2.2 The Outer Solar System: Icy Moons

1.2.2.1 The Icy Satellites

While on a larger scale than the ice shelves of Antarctica in terms of area, the icy moons of the solar system also experience widespread fracturing, which has been hypothesized to lead to some intriguing and sometimes bizarre landforms on those bodies. In a stellar system, the ice line marks the distance from the central star beyond which it is possible for hydrogen compounds to freeze into solid ice grains (e.g., *Kornet et al.* (2004)). In the proto-solar system, the greater abundance of large solid ice grains allowed for planetesimal accretion. These early planetesimals

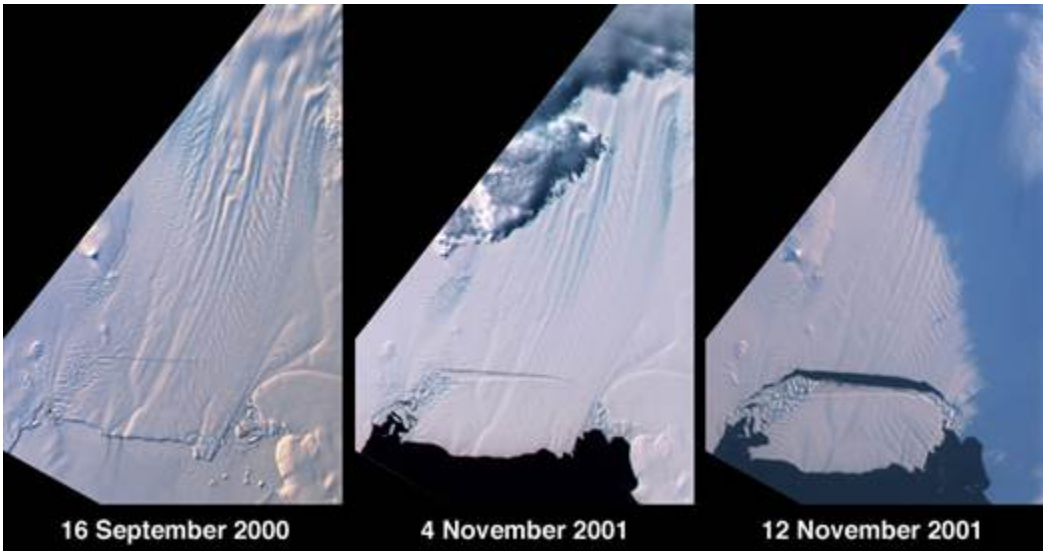

Figure 1.3: Series of images shows the initiation, propagation, and calving of an iceberg from the Pine Island Glacier in 2001. (a) a transverse-to-flow rift initiated from an array of cracks at the embayment wall; (b) 14 months later, the rift has propagated across about 3/4 of the ice shelf at a rate of approximately 15 m day^{-1}; (c) the rift ultimately propagates across the last 1/4 of the ice shelf's width between 4 November and 12 November of 2001, isolating an iceberg (42 $\times$17 km) that was then free to drift away. Representative of calving cycle observed there, as a similar series of events occurred in 2007, and again in late 2011 (it has propagated to within meters of severing the entire shelf width as of March 2013). This demonstrates that propagating rifts serve as the border for future icebergs as they approach the front. Image credit: NASA/GSFC/LaRC/JPL, MISR Team.

evolved into the large ice giant planets of the solar system. It is the ice line that is the boundary that separates the jovian planets from the terrestrial planets. The ice giants have a massive number of natural satellites, and unlike Earth and other terrestrial bodies, water ice rather than silicates, is the dominant constituent of the crusts of most of these bodies. Though the inventory has changed frequently in recent years thanks to improved observing capabilities—most notably by the Cassini spacecraft—it stands as follows: Jupiter has 67 satellites (the four largest are referred to as the "Galilean satellites": Io, Callisto, Europa, and Ganymede, the largest satellite in the solar system), Saturn has 62, Uranus has 27, and Neptune has 13. Pluto also lies beyond the ice line, and has five satellites. The icy satellites of the outer solar system are highly varied (Fig. 1.4). Despite the differences, however, there are common landforms that are observed on many of the moons. Fracturing processes are the most commonly observed feature across the satellites' surfaces, and specifically those observed on Enceladus (Saturn) and Europa (Jupiter) are the main focus of the work presented here. These moons are described in more detail in the following subsections.

1.2.2.2 Enceladus

Saturn's tiny moon Enceladus orbits Saturn at 180,000 km, between fellow moons Mimas and Tethys, outside of the famous rocky-ice rings. It is unusual in that it is among only a handful of moons and planets known to be geologically active. It is one of just three bodies in the solar system that exhibits on-going plume activity (*Porco et al.*, 2006). This likely relates to the fact that its surface is the most reflective in the solar system, with a bond albedo (total reflectivity) of 0.9 (*Verbiscer et al.*, 2007), about three times that of Earth (0.306) and almost 9 times that of the Moon (0.11). Its geological activity and water plumes are striking characteristics given that the global surface temperature is approximately 70 K and the moon has an effective radius of only 251 km (Fig. 1.5). Its orbital eccentricity is maintained by a 2:1

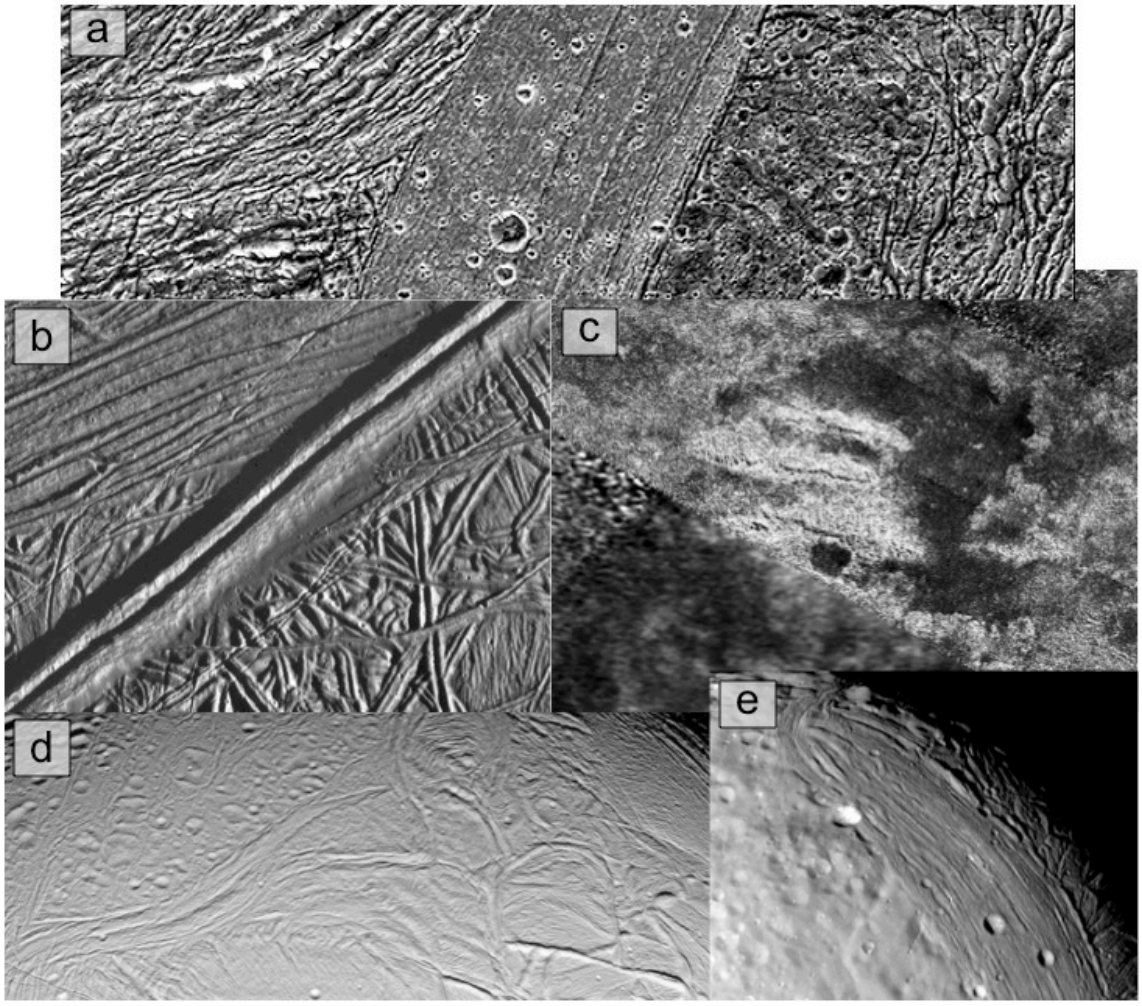

Figure 1.4: Various appearances of mountainous ridge features at icy moons. (a) "grooved terrain" at Ganymede; (b) ridges cross-cutting other fractures at Europa; (c) parallel mountain chains northwest of Xanadu on Titan; (d) compression folds in Enceladus' Northern hemisphere; (e) grooved terrain on Miranda. Image(s) credit: NASA/JPL/Space Science Institute

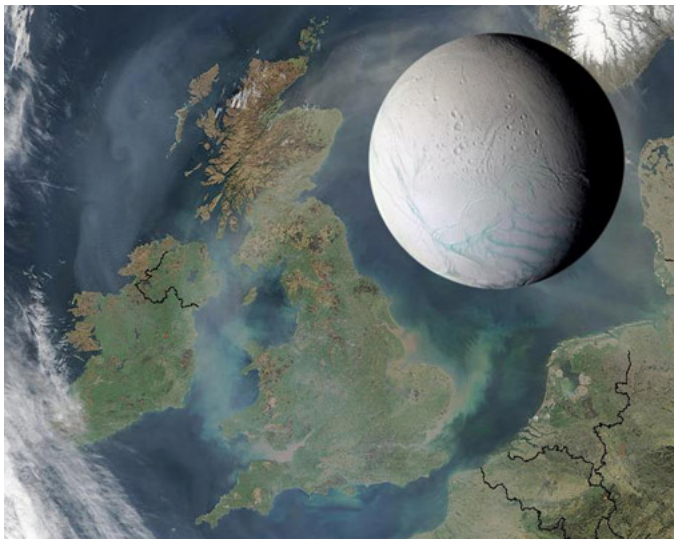

Figure 1.5: Enceladus' size compared to the familiar shape of the United Kingdom. It is Saturn's sixth-largest moon, and has a diameter of 505 km. Image courtesy: Image courtesy NASA/JPL/Space Science Institute.

resonance with Dione, which likely drives its tidal heating (e.g. *Porco et al.*, 2006). Another possible source of its lingering heat could stem from a change in its rotation. Like most Saturnian satellites, Enceladus is in a synchronous orbit—the same face is always pointed at Saturn—but studies of its shape have suggested that it was previously in a nonsynchronous 1:4 secondary spin-orbit libration (e.g. *Patthoff and Kattenhorn*, 2011).

Given its small surface area—about 800,000 km^2, about half the size of Alaska and almost twice the size of Ross Ice Shelf—there are a surprising number of different extensively tectonized terrains on the surface (*Pappalardo and Crow-Willard*, 2010). In contrast, another of Saturn's moons, Mimas, is of similar size but is tectonically inactive. Observations of Enceladus and its icy shell indicate a surface with a long history of activity and deformation, with regions of the surface ranging in age from primordial to geologically recent (e.g. *Porco et al.*, 2006; *Bland et al.*, 2007; *Barr*, 2008). This evidence of continued activity and the observation of active plume jets at the South Pole by the Cassini spacecraft suggest the possibility of a subsurface ocean, considered to be either regional (e.g. *Collins and Goodman*, 2007; *Tobie et al.*, 2008)

or global (e.g. *Patthoff and Kattenhorn*, 2011) in scale. The ice shell is likely decoupled from the interior of the satellite, with a thickness between 30-90 km, separated by either the global ocean or a warm, very ductile ice layer. The variation in surface features and ages suggest regional resurfacing events and processes are dominant, rather than processes on the global scale, and that a combination of viscous relaxation, cryovolcanism, and tectonic resurfacing may be responsible (*Passey*, 1983; *Squyres et al.*, 1982; *Kargel and Pozio*, 1996; *Spencer et al.*, 2009b; *Helfenstein*, 2010). Apparent regional tectonic resurfacing events are manifested in the varied appearance of portions of the globe (e.g., *Pappalardo and Crow-Willard* (2010); *Spencer et al.* (2009b) and others, Fig. 1.6). The Voyager 2 spacecraft first observed the surface of Enceladus in 1981, which resulted in the classification of five types of terrain in existence on the moon. Flyby observations by the Cassini spacecraft beginning in 2005 allowed the surface to be observed at better resolution, improving these classifications. Different terrain types on the surface are underlain by large regions of cratered terrain, likely the oldest sections of the moon; and smooth, relatively crater-free terrain, likely the younger sections of the surface. Old and young plains, called *planitiae*, are filled by extensive linear cracks, ridges, and scarps. Enceladus exhibits regions of compression ridges called *dorsa* (e.g., Fig. 1.7), and widespread extensional features appearing as large parallel rifts called *sulci* or trenches (called *fossae*). One of the most dramatic one of these is Labtayt Sulci, a 162 km-long, 1 km deep canyon (Fig. 1.7) (all features on Enceladus are named for people and places in *Arabian Nights*). Because of its approach geometry in 2005, early flybys by the Cassini spacecraft allowed for imaging of Enceladus' south pole, a region not viewed at all by Voyager 2. This unearthed the bizarre and mysterious terrain at the south pole.

The South Polar Terrain (SPT) is distinguished from the rest of the surface due to its noticeable lack of impact craters and relatively smooth appearance, the first clue that this section of terrain is younger than other parts of the moon (Fig. 1.8).

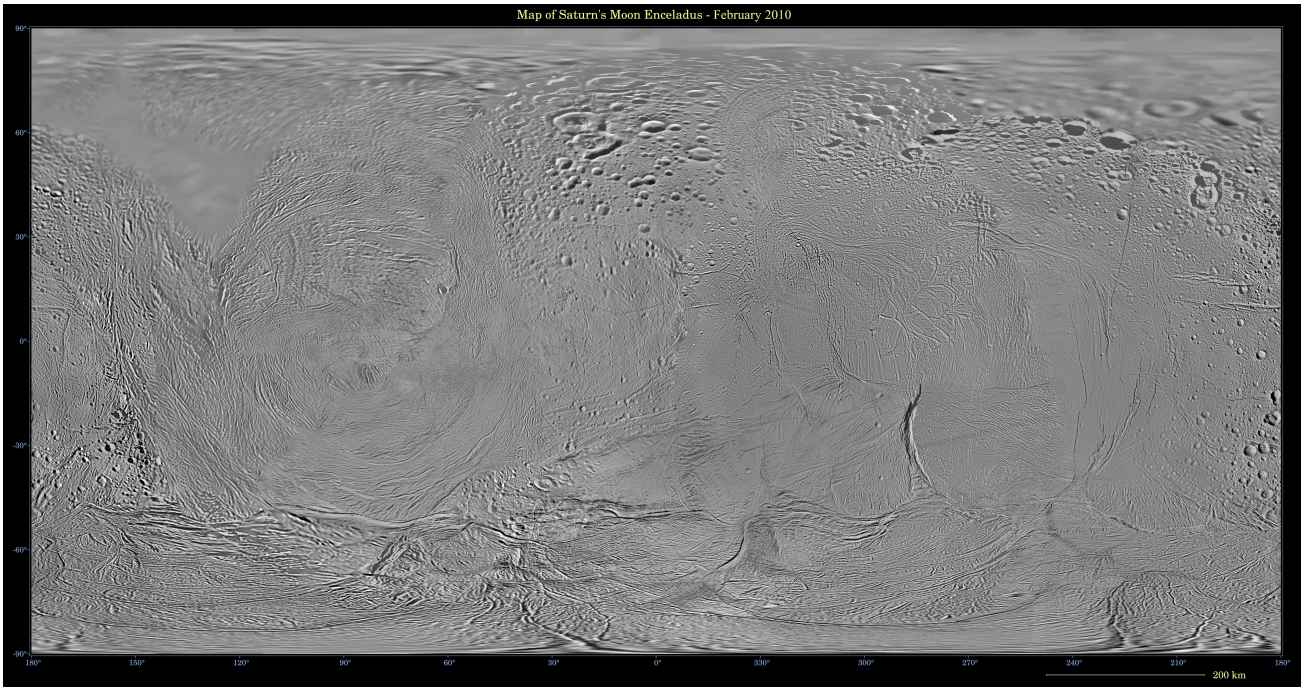

Figure 1.6: A global basemap mosaic of Enceladus created by NASA / Jet Propulsion Lab / Space Science Institute shows the variety of tectonized terrains on the small moon. Developed with images captured during the October and November 2009 Cassini flybys, July 2006 flybys, and the Voyager 2 flyby in 1981.

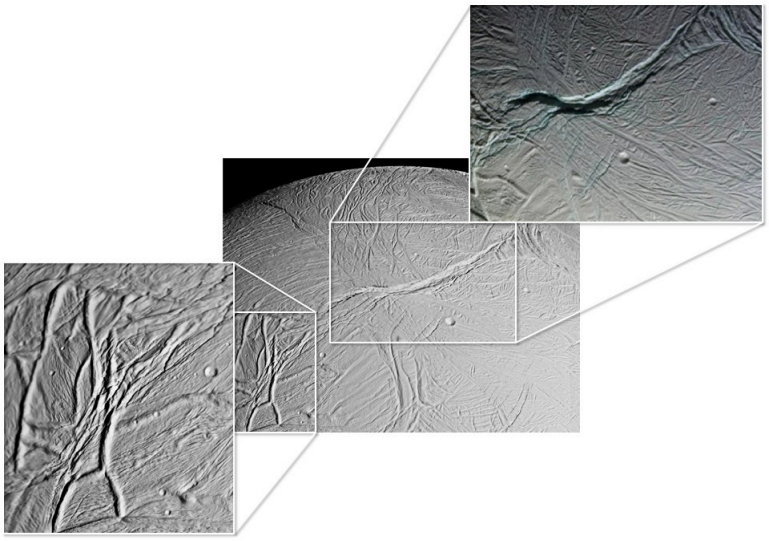

Figure 1.7: The trailing hemisphere of Enceladus showcases the Cufa Dorsa region (left) and Labtayt Sulci (right), which stems from the South Polar Terrain (upper right, middle image). Cufa dorsa features ridges thought to be the result of compressional tectonics, while Labtayt Sulci is a deep canyon hypothesized to be the result of extensional tectonics associated with the formation of the SPT. These images were captured October 5, 2008 during a flyby that took Cassini within 15 km of the surface. Image Credit: NASA/JPL/Space Science Institute

This young surface age is suggestive of current or recent resurfacing. Age estimates for the region range, but are fairly consistent between crater aging—younger than 100 million years to a few hundred thousand years (*Spencer et al.*, 2009b)—and ice shell convection models that suggest a possible surface age up to 10 Ma (e.g. *Barr*, 2008). The SPT is centered on the South pole and is bordered by a quasi-circular boundary feature at about 60°S latitude which appears to be a conglomerate of contiguous mountain chains with curved, poleward-facing cliffs. It has been interpreted as a convergent feature resulting from compressive stress along that boundary in the North-South direction (*Porco et al.*, 2006; *Helfenstein et al.*, 2011). Despite the uplift at the boundary, the "floor" of the SPT is relatively flat (*Schenk and McKinnon*, 2009), exhibiting ropy plains that are over-cut by four nearly-parallel, approximately 130 km fractures (the "tiger stripes"). The SPT region is located over a high-heat anomaly in the sub-surface, as observed by Cassini's Composite Infrared Spectrometer (CIRS), both unusual and unexpected. Heat is concentrated at the tiger stripes, with temperatures in the published literature established at approximately 167 K (*Spencer et al.*, 2006, 2009a,b), but could be up to approximately 190 K (e.g. *Spencer et al.*, 2008). Regions immediately adjacent to these fractures and along the uplift features at the boundary were observed by the Cassini Ion and Neutral Mass Spectrometer (INMS) and the Visible and Infrared Mapping Spectrometer (VIMS) to be the most recently exposed surface material (*Abramov and Spencer*, 2009). The observed active venting of water and trace gases that occurs at the South Pole is directly related to the tiger stripes; Cassini images show individual plume jets located along the fractures themselves (Fig. 1.8). These plume jets are the primary source mechanism for the maintenance of the E-ring (*Spahn et al.*, 2006). The secondary source is meteoric bombardment and particle escape from the surface. The E-ring is the very wide and diffuse outermost ring of Saturn made of of fine particles of ice and dust through which Enceladus orbits in the densest part (Fig. 1.8).

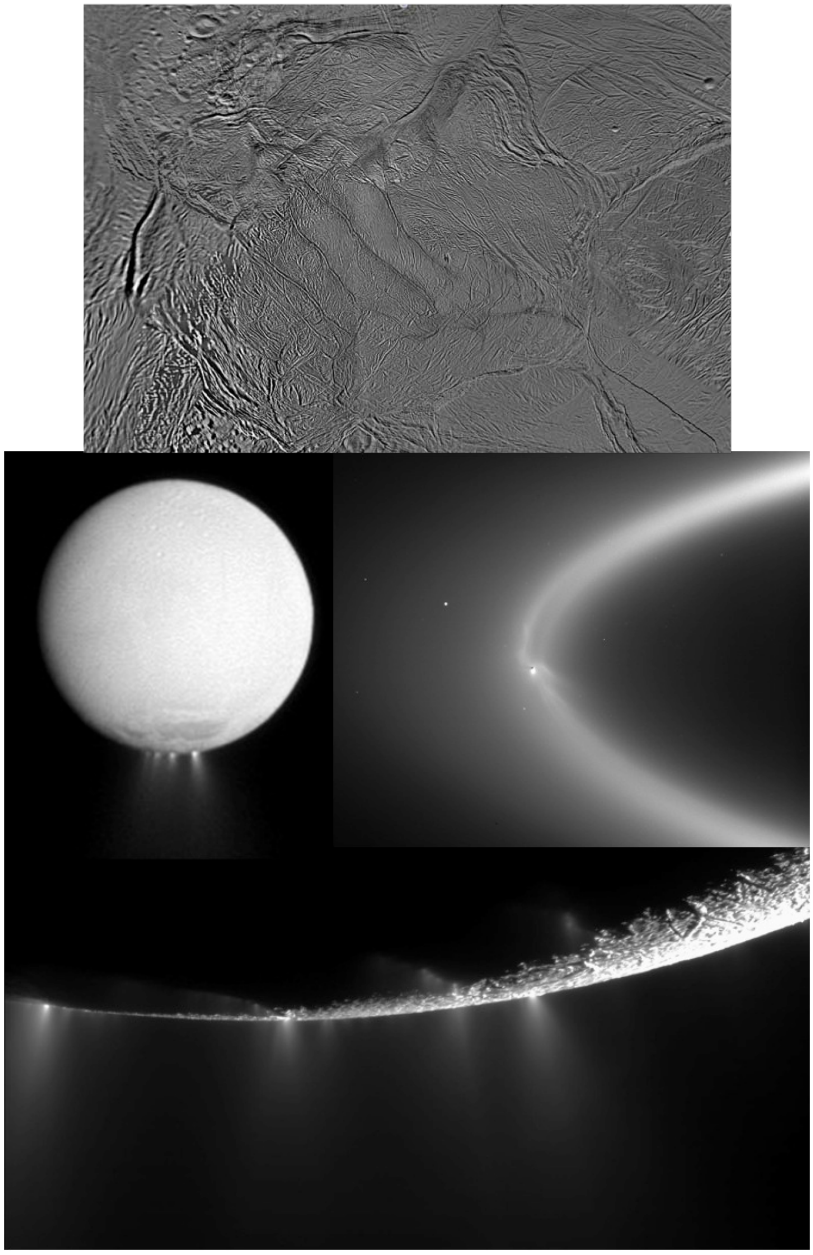

Figure 1.8: Enceladus vents subsurface materials into space. Top: The south pole of Enceladus, imaged during the 2009 flybys of Cassini. The four prominent tiger stripe fractures at the center are surrounded by a near-circular boundary of mountainous uplift. The entire region is depressed into the surface by 200-800 m. Middle left: A raw image captured on approach by Cassini shows the Sun-illuminated geysers from the south pole. Middle right: Enceladus' south polar vents release water and gas and supplies the E-ring of Saturn. Bottom: A close-up view captured in May 2012 of the jets set along the tiger stripe fractures themselves; one of the last images to be captured of the south pole of Enceladus by Cassini prior to this region going into shadow for the years to come. Image Credit: NASA/JPL/Space Science Institute

1.2.2.3 Europa

Europa is much larger than Enceladus, but is the smallest Galilean satellite with a radius of 1561 km. It is the sixth-largest moon (Earth's own Moon is fifth) and also one of the smoothest bodies in the solar system. It is a moon of great scientific interest due to the abundance of tectonic features on its surface (Fig. 1.9) and its subsurface ocean. It orbits Jupiter in a 2:1 resonance with its neighboring satellites Io and Ganymede. This particular scenario is called a "Laplace resonance" and is the only one currently known. The Laplace resonance causes the orbits to remain eccentric, and is the driver behind the high level of tidal heating and stress in these moons (*Greenberg et al.*, 1999). Notably, Io is the most volcanically active body in the solar system (including Earth) (e.g. *Lopes and Carroll*, 2008). At Europa, tidal heating is considered to be the driving mechanism by which the subsurface ocean remains liquid (e.g. *Squyres et al.*, 1982; *Ross and Schubert*, 1987), and arcuate lineaments ("cycloids") on the surface betray tidal stress patterns (e.g. *Hurford et al.*, 2007a; *Groenleer and Kattenhorn*, 2008; *Rhoden et al.*, 2010).

Europa's surface was first observed in images captured by the Galileo spacecraft (e.g. *Belton et al.*, 1996; *Greeley et al.*, 2004). Differing tectonic signatures showcase variable links between global stress mechanisms, interior structure, and surface geology. Europa exhibits a multitude of landform types, including fractures, ridges, bands, folds, domes/lenticulae, chaos terrains, and impact craters. The two main sources of global stress at Europa are proposed to be non-synchronous rotation of the shell and diurnal tidal variations, which are highlighted by the cycloid fracture chains on its surface. *Prockter and Patterson* (2009) suggest that ridges and bands, the most ubiquitous structure types, initiate as fractures and subsequently modified by processes associated with ice shell deformation due to tidal stress and nonsynchronous rotation, among others (*Greeley et al.*, 2004). The fracture ridges are ubiquitous across the surface, and several models have been suggested for the formation of ridge

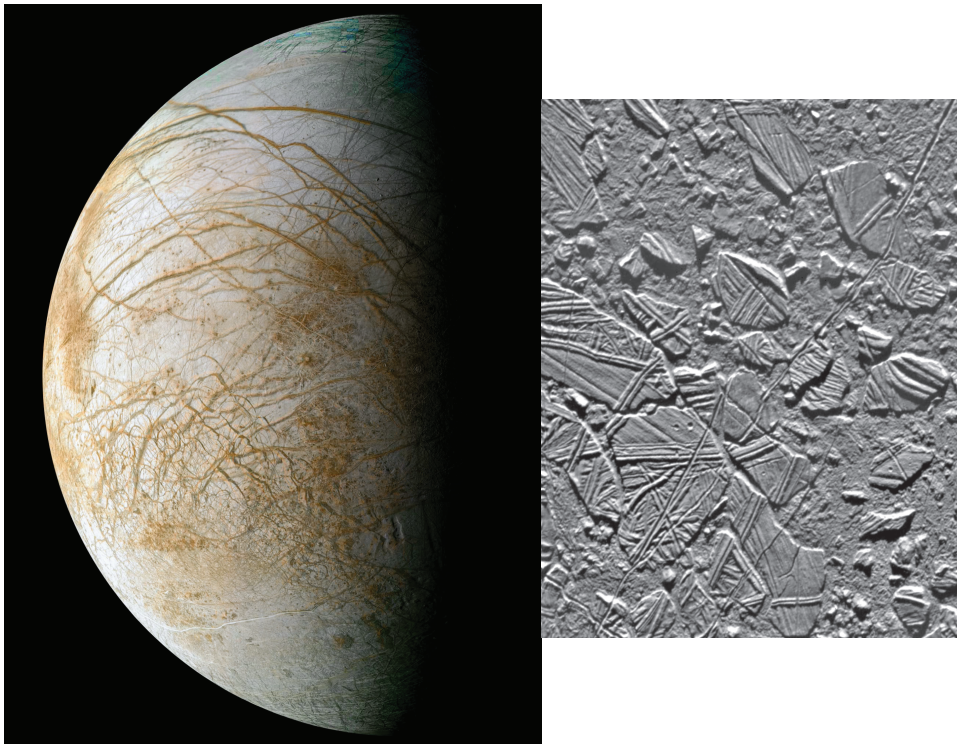

Figure 1.9: Patterns of fracturing cover Europa. Reddish linear to curvilinear features are observed - the reddish-brown material is a non-ice contaminant that colors Europa's frozen surface, likely from subsurface interaction or impactor contamination of the surface. Data used to create this view were acquired by the Galileo spacecraft in 1995 and 1998. Right image shows an example of the "chaos terrain" called Thera Macula. This terrain is found distributed over Europa's surface. Image credit: NASA/JPL/Ted Stryk

morphology, but the most attractive features shear deformation in a primary role. Bands are not as ubiquitous as ridges, but are common across regions of the surface. Since the Galileo mission, morphological studies of these bands have shown that bands are extensional in origin (referred to as "pull-apart" bands in the literature) and are commonly associated with shear (e.g. *Schenk*, 1989) (Fig. 1.10). Another surface type associated with fracturing or tectonics in the icy lithosphere is the "chaos terrain". Chaos terrain, a variation of which is also found on Mars (e.g., Aureum Chaos region), is an area in which a mix of ridges, fractures, and jumbled plains appear entangled with each other (Fig. 1.9). The complexity of these regional formations have made it difficult to determine the individual mechanisms by which they are formed. Theories have ranged between crust-penetrating impacts (*Ong et al.*, 2004) to crustal thinning and brine intrusion from near-surface reservoirs (*Schmidt et al.*, 2011), but such hypotheses remain unconfirmed at present due to the lack of spacecraft or instrumentation dedicated to observing Europa's subsurface, or even its surface for extended periods of time. This may be remedied in the next two decades with the (proposed) 2022 launch of the European Space Agency's (ESA) JUpiter Icy moon Explorer (JUICE) mission, with a planned tour of Ganymede, Callisto, and Europa, when it reaches the Jupiter system in 2030 (planned).

While it has not been directly observed and there is no certain evidence (yet) for current surface activity, it is widely believed that Europa remains tectonically active today (*Collins et al.*, 2009). The observed number of large impact craters on Europa (>20 km) implies a surface age of approximately 60 Myr as modeled by *Levison et al.* (2000); *Zahnle et al.* (2003); *Schenk et al.* (2004). Another way of determining surface age comes from estimates of ice sputtering by impacting energetic particles. The Galileo Energetic Particle Detector (EPD) collected measurements and estimates of water particle sputtering rates were suggested by both *Ip et al.* (2000) and *Cooper et al.* (2001), ranging between 1.6 and 56 cm Myr^{-1}. High-resolution imagery shows

Figure 1.10: False-color image of Europa's highly fractured and ridged surface. The complicated chronology mapping of ridges and cracks points to considerable geological activity. Mosaic created by images captured by the Galileo spacecraft. Image credit: NASA/JPL

that Europa's oldest terrain, the ridged plains, have vertical scales on the order of tens of meters. Using this information, it has been put forward that since topography has not yet been completely erased, then Europa's surface must be only approximately 50 Myr old. In this case, it is likely that Europa remains active today, but would require a longer observing campaign, since the opportunities to search for activity during the Galileo mission were limited (e.g. *Phillips et al.*, 2000).

1.3 Planetary Tectonics

The study of tectonics—from the Greek *tektos*, or "builder"—concerns the development of landforms and surface features from the deformation of a planetary crust. While it began as a controversial theory (later accepted based on marine ship-borne experiments), the study of tectonics on the Earth and planets has become commonplace with the advent of satellite remote sensing capabilities and improved telescopic observations. Because deformation of the crust is a physical response to subsurface forces and processes, the study of tectonics often allows a window into interior pro-

cesses that are otherwise shielded from view.

The ability to interpret tectonic landforms on the terrestrial planets and satellites is based in our understanding of tectonic landforms on our own planet Earth. Scientists have come to the realization that the tectonics of the Earth are unique in the solar system in that it occurs by the movement of localized lithospheric plates. Most other terrestrial bodies that exhibit tectonics, including Earth's Moon, behave largely as a single continuous shell. However, each of the terrestrial planets and moons showcase distinctive styles of tectonics, expressing different paths of interior and crustal evolution. In addition to the terrestrial planets and similarly rocky moons, the icy satellites of the outer solar system also exhibit signatures of tectonics.

Despite major differences in properties between ice and rock, most studies of tectonic features on the icy moons are comparative in nature, depending on Earth analogs to understand various features of the moons, such as normal faulting, folds, graben, mountain chains, tilt-block complexes, and basins (*Collins et al.*, 2009). Overall, extensional signatures are observed on every outer planet satellite, but surface contraction and/or compressional features are less common (thus far). This has been linked to the likelihood of global subsurface oceans that cool and freeze, causing thickening of the floating shell and therefore extensional stress in the upper lithosphere (e.g. *Nimmo*, 2004; *Manga and Wang*, 2007; *Collins et al.*, 2009; *Rudolph and Manga*, 2009).

In general, across the spectrum of icy satellites, tides are supremely important to surface and subsurface evolution. The stress field that lead to the formation and global features are often controlled or modulated by changes in the tidal figure of the body. The evolution of a satellite's orbit over time suggests that formation mechanisms may be different from maintenance or modifying mechanisms at work today, since we cannot assume that any satellite has remained in a steady state with respect to tidal stress and energy input due to tidal dissipation.

The tidal flexing and tidal dissipation are likely key players in the geological evolution and ongoing activity at many of the moons. A non-zero orbital eccentricity results in ongoing deposition of orbital energy into the interiors of the satellites on a timescale much shorter than the eccentricity damping and dissipation timescales. Tidal effects on the satellites, especially in the Galilean satellites of Jupiter, have endured over long geological timescales, mostly due to the Laplace resonant orbit between Europa, Io and Ganymede. More surprising is the continued tidal effects on satellites like Enceladus, with a small eccentricity and a focused tidal heating spot at the south pole which has yet to completely dissipate its tidal heat (e.g. *Howett et al.*, 2011). In the absence of a specialized resonant orbit like that of the Galilean moons that enhances and maintains eccentricity, tidal dissipation has the effect of circularizing an orbit relatively quickly, delivering energy into the satellite interiors. While we can estimate the energy dissipation into the satellite interior, it represents a global total, and contains no information on how or where the tidal dissipation occurs. A local example is exemplified by the asymmetric high heat spot at the south pole of Enceladus; globally, Europa is more homogenous than Enceladus in terms of heat distribution, though hot spots are theorized to exist leading to localized thin-shell regions (e.g. *Schmidt et al.*, 2011). A key player in the tectonics of the moons' surfaces is the ability to characterize the heat production and distribution in the subsurface, topics that remain not well understood.

1.4 Comparative Planetology

It is currently impossible to complete in-situ observations at the icy moons, so for planetary ice observations to be properly interpreted, it is useful to obtain an understanding of fracture and deformation processes in terrestrial ice. While laboratory experimental measurements can provide data concerning ice behavior under certain conditions, it is essential to gather insight into glaciological processes to provide a

grasp on phenomena such as rift propagation and ice deformation on the larger geophysical scale. One of the most striking features of the icy moons is, despite the fact that the moons are so varied, topographically-similar ridge and fracture formations are widespread. These features are, at least at first glance, similar to the rift systems on Earth and ice flow morphology prevalent in Antarctic ice shelves. Moreover, ice shelves may provide an apt analogy to the behavior of an icy crust atop a subsurface ocean. The radical difference in temperature and pressure between icy moons and terrestrial ice sheets suggests caution in making comparisons. However, two observations provide us with optimism in this interpretation: first, laboratory and field measurements of glacier ice indicate that strength and fracture properties are remarkably insensitive to temperature over the range of temperatures we expect to encounter. Second, heat flow calculations suggest the bottom layer of the icy shell is either at or close to the pressure melting point. The implication is that the bottom portion of the ice shell has a temperature comparable to terrestrial ice sheets.

Observations of Earth-bound regions serve not only to provide background in large-scale processes, but also provide an important view of how physical properties of material—in this case, ice—can affect the formation of features. With the absence of direct observation at the moons, we can employ analog observations to observe how these features interact with each other also. *van der Veen* (1998a) and *Hulbe et al.* (2010) showed that crevasses interact and alter stress fields within the surrounding ice. These terrestrial observations of ice behavior are essential to obtaining a firm platform from which to hypothesize on formation mechanisms at the icy moons. Imagery of many icy moon surfaces has revealed the ubiquity of near- to sub-parallel ridge and rift features across many moon surfaces. Many of these features are reminiscent of those that we observe in Earths rocky crust and ice sheets. From the standpoint of comparative planetology, we can study these lineament features through the "looking-glass" of terrestrial observations to better constrain theories of formation.

1.5 Objectives: Questions Addressed in this Dissertation

Somewhere, something incredible is waiting to be known.

– Carl Sagan

Relevant to both Earth and planetary processes, we investigate the driving mechanisms and processes behind the fracture of ice. Still a poorly understood phenomenon, this lack of understanding leads to an undermining of effective models to accurately predict future ice shelf evolution. This affects the ability of climate models to accurately predict changes in climate in the coming centuries. In addition, a lack of understanding of the mechanisms driving fracture propagation lead to large uncertainty in the ability to accurately characterize planetary evolution. With the advent of satellite imagery, we study both Earth and planetary ice, and in this dissertation we seek to address the following questions:

- How does ice fracture? What drives the propagation of fractures in ice?
- What aspects or drivers of rift propagation can we observe in the ice shelves of Antarctica? Is rift propagation related to environmental changes? What other forces may contribute to activity?
- What are the implications from these Earth-based studies for the fractured ice shells of the outer planet satellites? Can we successfully employ comparative planetological studies to explain features at the icy moons?

In pursuing the answers to these questions, we seek to advance our understanding of rifting processes in ice both on Earth and on the planets, and in the long term, contribute to the growing field of comparative planetology and the application of Earth analogues to study extra-terrestrial bodies. To do so, this dissertation discusses models developed for both Earth and planetary ice, and incorporates Earth observations in order to provide a realistic basis for our conclusions.

1.6 Dissertation Overview

Chapter 2: In Chapter 2, we discuss the deformation and fracture of ice, to provide the necessary theoretical background for the chapters that follow. We present background on both terrestrial and planetary ice and point out similarities and differences that are important to emphasize in comparative studies like the one presented in this dissertation.

Chapter 3: Iceberg calving is an important mass loss process from Antarctica that remains poorly understood. The precursor to calving from ice shelves is the formation of through-cutting rifts that initiate and propagate for decades before eventually isolating an iceberg. We have observed 72 rifts in 13 Antarctic ice shelves using Moderate-resolution Imaging Spectroradiometer (MODIS) and Multi-angle Imaging SpectroRadiometer (MISR) images acquired over a decade (2002-2012) to provide a large sample of rifts around the continent, in varying glaciological and oceanographic settings. Thirty-four (47%) of the observed rifts remained dormant for the entire decade; the remaining 38 rifts exhibited episodic propagation, with varying recurrence intervals. Only seven of the rifts propagated continuously over the decade: five on the Amery Ice Shelf, one on the Filchner Ice Shelf, and one on the Ronne Ice Shelf. Additionally, eight rifts around the continent propagated continuously for at least five consecutive years before stopping. These 15 continuously-propagating rifts were all initiated at the ice shelf fronts, possibly linking this type of rift to the observed increase in propagation activity when compared to non-front-initiated rifts. The remaining 23 rifts propagated episodically with a much longer recurrence interval, resulting in large "sudden burst" propagation events once or twice in the entire decade. We determined that the arrival of tsunamis at the Antarctic coast caused propagation events of front-initiated rifts, occasionally leading to iceberg calving. We hypothesize that front-initiated rifts are particularly sensitive to the wave impact since it leads to pressure propagation within the rift and therefore increased horizon-

tal pressure on rift walls. Our dataset represents the most geographically extensive record of rift propagation to date, and provides a benchmark against which we can compare future rift activity. This chapter has been accepted into the Journal of Geophysical Research (*Walker et al.*, submitteda).

Chapter 4: We investigated rift propagation in five rifts within 30 km of the calving front of the Amery Ice Shelf, East Antarctica using Moderate resolution Imaging Spectroradiometer (MODIS) and Multi-angle Imaging SpectroRadiometer (MISR) imagery. For the period 2002-2012, we find that all five rifts propagated, but with a complex spatio-temporal pattern of variability. Temporal variability in rift propagation is dominated by intermittent bursts of propagation. These propagation events are not synchronous across all five rifts nor do the timing of propagation events exhibit any correlation with observed proxies for environmental forcing (e.g., atmospheric temperatures, sea-ice extent). However, we do observe a correlation between rift propagation and tsunami runup. We postulate that the pronounced activity observed relative to other ice shelf rift activity is due to the fact that the Amery Ice Shelf is approaching its most extended position prior to a large calving event in 1963-64 and that the highly dynamic propagation we observe is the precursor to the next major calving event. This chapter has been submitted to the Journal of Geophysical Research (*Walker et al.*, submittedb).

Chapter 5: The absence of many craters and the presence of smooth, young surfaces indicate that Enceladus and Europa have likely been resurfaced through recent or ongoing tectonic and volcanic activity. For interior materials to erupt or otherwise flow out onto the surfaces of these satellites, fractures would have to vertically penetrate the ice shell to the depth of a subsurface reservoir or ocean. Based on observational studies of Earth ice, the fact that the shells are highly fractured affects the depth to which a fracture could penetrate under tensional stresses. An additional factor in the penetration of the ice shell is whether or not basal fractures form, and if

they are filled by liquid water. We use a linear elastic fracture mechanics (LEFM) approach, supported by a Nye zero-stress estimation, to model the vertical propagation of fractures in the ice shells, which are subjected to tensional and overburden stresses. We consider a range of estimates for the thickness of the layer of ice that behaves elastically to determine what shell depths may be fully ruptured by a given tensional stress. The inclusion of multiple closely-spaced fractures in the model of fracture propagation has the overall effect of lessening the amount of stress concentrated in a fracture. We find that tensional stresses between 1-3 MPa may fully fracture the structurally-compromised shell of Europa if the elastic thickness is $\leq$1 km. In the case of Enceladus, tensional stresses between 1-3 MPa may completely crack shells of 11-22 km elastic thickness.

Chapter 6: The South Polar Terrain (SPT) of Saturn's moon Enceladus is a mysteriously active region that exhibits intriguing tectonic signatures and widespread fracturing. The central region of the nearly-circular SPT is depressed into the surface by a few hundred meters and bounded by a ring of cliffs roughly 1 km high. In this study, we investigate whether this depression and surrounding mountainous uplift is consistent with the morphology of terrestrial rift basins and the possibility that the SPT could have formed during a tectonic event analogous to those of such rift basins on Earth. Using three mechanical models of basin formation, we compare our predicted topography of the SPT with observed topography of the region. The first of three models we consider assumes crustal stretching by factor β, and predicts a basin depth of roughly 600 m, closely matching previously published estimates of the depth at the SPT. Models of extension and compression, assuming an elastic response in the ice crust, predict best-fit mountain uplift of roughly 1820 m and 1130 m, respectively. Our preferred model suggests that the icy shell in the SPT has been stretched, but the extension is (partially) balanced by compression along the edges of the basin leading to the uplift of the mountains along the boundary, thereby implying that the SPT

may have a tectonic origin analogous to that of a terrestrial basin. This chapter has been published in the Journal of Geophysical Research (*Walker et al.*, 2012).

Chapter 7: In Chapter 6 we summarize what we have learned from the work covered in the previous 4 chapters and discuss the bigger picture. We also discuss future directions necessary to continue advancing such studies of astro-glaciological and comparative planetological interest.

Appendix A: Appendix A showcases our work to migrate a flexure model commonly carried out in a Cartesian geometry to a spherical shell geometry. We also discuss how the results shown in Chapter 6 change significantly between the two, motivating our use of the spherical model for flexure at Enceladus. We also discuss the spherical shell implications for bending and membrane stresses, and how they might affect results in Chapter 5 in terms of the augmentation of the stress intensity factor.

Appendix B: In Appendix B we show an experimental model that was developed to test compressional modes for Enceladus' ice shell. We used a granular model of ice to complete a thought experiment in creating the icy mountain belts of Enceladus by marrying this ice shelf model with simple models of tectonic mountain formation. In this work we attempt to show the ways in which the mountains surrounding the SPT may have formed; very few studies have addressed the compressional features on icy moon surfaces. This Appendix is part of on-going work on the subject.

Appendix C: In Appendix C we discuss work completed at the Jet Propulsion Laboratory (JPL) during the summer of 2010 under support by the Michigan Space Grant. The laboratory work took place in the Ice Physics Lab and Planetary Tides Simulation Facility and focused on fatigue testing of ice samples. We created cylindrical samples of pure water ice through compaction of a variety of ice grain sizes. These samples were then subjected to loading that mirrored the loads placed on the icy moons throughout their orbit (alternating compressive and tensile stress)

for weeks at a time. Through this testing we could determine an effective viscosity for the ice, and also study the micro-structure of the ice and how it changed over time using a cryo-microscope before and after testing. This Appendix summarizes the work completed that summer.

CHAPTER II

Theoretical Background: Deformation and Fracture of Ice

2.1 Rheology of Ice

"Rheology" is a segment of study in the discipline of continuum mechanics which relates how materials flow to the state of stress, and comes from the Latin *panta rhei*, meaning "everything flows". The rheology of ice is approximated using a range of flow laws (constitutive relations), the validity of which depends on timescale, stress and temperature, and grain size of ice. On short timescales (on the order of seconds to days), glacier ice deforms as a solid elastic material. Over longer timescales (on the order of years) ice behaves more like a viscous fluid, evident by the observation that ice flows, e.g., glaciers (e.g. *Paterson*, 2000). The fracture of ice, in itself, occurs over a range of timescales; fracture initiation or propagation event can occur in seconds to minutes or less, while the propagation of a rift across a large section of an ice shelf can take place for years or decades. Ice behaves both elastically and viscously, dependent upon the timescale and loading, and different fracture mechanics models apply in the elastic, ductile and plastic cases.

2.1.1 Planetary perspective: Consideration of ice as planetary bedrock

Ice acts as the "bedrock" of the outer solar system, and so the rheology employed in planetary tectonics models of the terrestrial planets may be altered when considering tectonics in ice. Water ice (planetary and Earth's ice sheets and glaciers) has several differences when compared to silicate materials that make up the crusts of the terrestrial planets and moons. Unlike the relation between solid rock and molten rock, solid ice is less dense than liquid ice. Therefore, eruption of water onto the surface necessitates the consideration of cryo-volcanic processes in the subsurface. Additionally, the viscous flow timescales for icy bodies are much shorter than those in silicate bodies, as ice close to its melting point flows much more readily than nearly-molten rock (*Collins et al.*, 2009), i.e., it has lower viscosity. In addition to being more ductile than silicate rock, ice is also less rigid and is subject to brittle failure at much lower stresses than rock (e.g. *Weeks and Cox*, 1984). However, just as in silicate materials, stressed ice can respond in idealized regimes: (1) elastic, at low stresses and strains; (2) ductile (viscous creep) at higher temperatures and/or lower strain rates; (3) visco-elastic, in which a material has both elastic and ductile properties over intermediate timescales.

2.2 Linear Elastic Fracture Mechanics

Linear elastic fracture mechanics (LEFM) assumes that fractures initiate from sharp "starter" cracks always present in the materials. The criterion to decide if a crack will propagate can be evaluated by studying the stress concentration at the crack tip in comparison to a material property called the fracture toughness. Fig. 2.1 shows the three principle modes of fracture (e.g. *Lawn*, 1975). Mode I propagation, also called "opening mode", occurs when a fracture is subjected to tensile stress normal to the fracture plane, and displacement of the fracture walls occurs in the

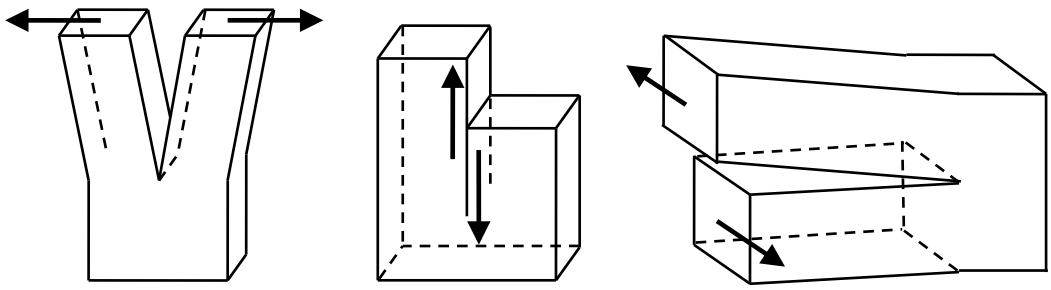

Figure 2.1: Three modes of fracture: (a) Mode I fracture: tension normal to the fracture plane. (b) Mode II fracture: sliding mode due to shear loading. (c) Mode III fracture: tearing mode due to out-of-plane shear loading.

direction of maximum tensile stress (i.e., also perpendicular to the fracture plane). Mode II propagation, called "sliding mode", occurs upon shear loading in the fracture plane. In this case the displacement of the walls occurs parallel to the fracture plane (and normal to the fracture tip). The third mode of fracture, Mode III, is called "tearing mode" and results from out-of-plane shear loading, where shear stress acts parallel to the fracture plane and parallel to the crack front. Fractures can also propagate as mixed-mode fractures. In this dissertation, we are concerned with mode I fracture only. In linear elastic theory, under applied loads, stresses concentrated at a crack tip are infinitely large, creating a singularity (e.g. *Broek and Rice*, 1975; *van der Veen*, 1998a). In reality, plastic deformation occurs around the crack tip to limit elastic stresses, but as long as this area is small compared to the crack length, the theory of linear elastic fracture mechanics (LEFM) can be applied (*Gdoutos*, 1993). The stress concentration around the crack tip is quantified using a variable called the stress intensity factor. It is modulated by the material and structural setting in which the defect exists and the mode of fracture present.

In LEFM, the stress field, σ_{ij} near the tip of a sharp crack can be expressed as (*Broek and Rice*, 1975; *van der Veen*, 1998a; *Tada et al.*, 2000)

$$\sigma_{ij} = \frac{K_m}{\sqrt{2\pi r}} f_{ij}(\theta) + ... \tag{2.1}$$

$f_{ij}(\theta)$ is a known dimensionless function of θ, the angle with respect to the crack plane (dependent on loading and fracture geometry), r is the distance from the crack tip and the higher order terms on the right hand side are small compared to the square root of r singularity which dominates the near-crack stress field. Plastic deformation occurs to bound the singularity in the limit where $r \to 0$. The size of this plastic region, distance r_p from the crack tip, can be calculated using the plastic yield strength of a material, σ_y, and Eq. 2.1 and expressed as (*Broek and Rice*, 1975; *van der Veen*, 1998a)

$$r_p = \frac{K_m^2}{2\pi\sigma_y^2}, \tag{2.2}$$

r_p represents the distance at which elastic stress equals the plastic yield strength of the material. Hence, at distances less than r_p, plastic deformation occurs to limit elastic stress in that region. In both Eqs. 2.1 and 2.2, K_m represents the stress intensity factor, with a subscript m representing the mode of fracture (I, II, III). The stress intensity factor has the dimensions of stress times square root of length (Eq. 2.1), and is defined generally for each mode of fracture:

$$K_I = \lim_{r\to 0} \sqrt{2\pi r}\sigma_{yy}(r, 0), \tag{2.3}$$

$$K_{II} = \lim_{r\to 0} \sqrt{2\pi r}\sigma_{yx}(r, 0), \tag{2.4}$$

$$K_{III} = \lim_{r\to 0} \sqrt{2\pi r}\sigma_{yz}(r, 0). \tag{2.5}$$

A crack will propagate when the net stress intensity factor exceeds a critical value called the critical stress intensity factor, K_{IC}. In glacier ice, K_{IC} has been measured and is typically on the order of 0.15 MPa $m^{1/2}$ (*Rist et al.*, 2002). In various planetary ice studies, a range of values between 0.1-0.4 MPa $m^{1/2}$ have been used citing the

earlier work of *Rist et al.* (1996).

2.3 Viscous behavior of ice

2.3.1 Viscous behavior in terrestrial ice

Over long timescales, elastic deformation in ice is largely negligible for many glaciological processes. However, fracture occurs over a variety of timescales, and so the distinction between elastic and viscous behavior is an important divide, as the LEFM method described above relates only to elastic behavior in the ice. The viscous rheology of ice is less known. The flow law most commonly used for terrestrial ice sheets is a power law (*Glen*, 1952; *Nye*, 1957) and is expressed as

$$\dot{\varepsilon}_{ij} = A\tau^{n-1}S_{ij}, \tag{2.6}$$

where n is the flow-law exponent, A is a rate constant, P is the pressure and τ is the second invariant of the stress tensor, which can be written

$$2\tau^2 = s_{11}^2 + s_{22}^2 + s_{33}^2 + 2(s_{12} + s_{13} + s_{23})^2. \tag{2.7}$$

In both Eq. 2.6 and 2.7, S_{ij} is the stress deviator and is expressed as:

$$S_{ij} = \sigma_{ij} - P\delta_{ij} \tag{2.8}$$

Alternately, Eq. 2.6 can be inverted to express the stress deviator in terms of the strain rate instead:

$$S_{ij} = \frac{1}{A\tau^{n-1}}\dot{\varepsilon}_{ij} \tag{2.9}$$

and since stress deviators are related to strain rates by an effective viscosity η_{eff}

(e.g. *Van der Veen and Balkema*, 1999), Eq. 2.9 gives

$$\eta_{eff} = \frac{1}{A\tau^{n-1}}. \tag{2.10}$$

It is most common in the published literature to use a flow-law exponent of $n = 3$, though $n = 3.5$ may be more appropriate for stresses of the order of hundreds of kPa (*Glen*, 1952). At lower stresses, *Hutter and Hughes* (1984) showed that $n = 1$ is more appropriate, which is called a "Newtonian rheology". This is often used in models at the icy moons. It is also possible for much higher stresses, values of the order of $n = 10$ would apply. More recently, *Goldsby and Kohlstedt* (2001) proposed a grain-size dependent flow law, one that is most often employed in models of ice flow at the icy moons.

2.3.2 Viscous behavior in planetary ice

The ice comprising the shells of the icy satellites exists at much lower temperatures and, at least at the upper layers, at lower pressure than terrestrial ice, and acts as the "bedrock" in the outer reaches of the solar system. At deeper levels within the crust, the ice is harder to characterize (likely Ice II or III). The icy shells undergo a range of stresses throughout their evolution, from large tectonic or orbit stabilization stresses on the order of 1-10 MPa, to relatively low stresses from tides, on the order of 100 kPa. As above, laboratory investigations have sought to clarify the deformation mechanisms responsible for terrestrial ice sheet flow have pointed to a composite flow law that can match viscosity measurements from terrestrial ice and previous laboratory measurements (*Collins et al.*, 2009). The composite flow law most often used in planetary ice deformation studies differs from the common terrestrial expression, and takes into account four deformation mechanisms (*Goldsby and Kohlstedt*, 2001): diffusion (diff), grain boundary sliding (gbs), basal slip (bs), and dislocation creep (disl).

Experimental setup and data acquisition for studies regarding these mechanisms at the icy moons is described in Appendix C.

The total rate of deformation can be expressed as the sum of strain rates due to the four individual creep mechanisms,

$$\dot{\varepsilon}_{tot} = \dot{\varepsilon}_{diff} + \dot{\varepsilon}_{disl} + \left(\frac{1}{\dot{\varepsilon}_{GBS}} + \frac{1}{\dot{\varepsilon}_{bs}} \right)^{-1}. \tag{2.11}$$

Grain boundary sliding and basal slip are collectively called grain-size-sensitive creep and both are expected to operate simultaneously to permit deformation (*Durham et al.*, 2001). The mechanism at work depends on the specific stress and temperature conditions considered. The strain rate for each deformation mechanism can be described by the general expression:

$$\dot{\varepsilon} = A\sigma^n d^{-p} exp\left(-\frac{Q + PV}{RT} \right). \tag{2.12}$$

Here, $\dot{\varepsilon}$ is the resulting strain rate for a given mechanism, σ is the applied stress, d is the grain size, A, n, and P are experimentally-derived constants, Q is the activation energy, V is the activation volume, R is the gas constant, P is the pressure and T is the temperature. Several different mechanisms can be operating at the same time, which is why the total strain rate (Eq. 2.11) is a function of the individual strain rates (e.g. *Goldsby and Kohlstedt*, 2001).

The deformation mechanism at work in the ice is determined by the applied stress and temperature for a given grain size (e.g., Fig. C.5 in Appendix C). Diffusion creep occurs at lower stress and higher temperature and results in Newtonian flow ($n = 1$). Basal slip and grain boundary sliding are the dominant mechanism under higher stress and lower temperatures and result in non-Newtonian flow ($n = 2$). At especially high stresses, dislocation creep dominates and results in strongly non-Newtonian flow.

Most studies suggest that stresses and strain rates within the warmer interiors of

the satellites are low, and so the most likely deformation mechanism there is diffusion creep (*McKinnon*, 2006; *Moore*, 2006). Closer to the surface, it is more likely that other mechanisms are at work due to higher stresses present. The viscosity is dependent on grain size, another parameter that is very poorly constrained at the icy moons. It has been accepted in simpler models of tectonic deformation that the ice has Newtonian viscosity near its melting point. More complex models have been developed that take into account non-Newtonian and viscoelastic behavior in the ice (e.g. *Dombard and McKinnon*, 2006a,b) by assuming an effective composite strain rate.

2.4 Rheological implications at the icy satellites

The ability to properly interpret landforms and features on the icy satellites depends mainly on the response of the icy material to tectonic and other stressors like tides. Hence, developing an understanding of the rheology of ice and icy-rock mixtures is essential. Rheological applications at the icy moons are relevant not only to improve understanding of surface processes, but also the interior structure, another aspect of icy moon study that remains unclear. While observable temperatures at the surface paired with small overburden pressures in the shallow subsurface suggest that the upper layer behaves elastically, higher temperatures at depth likely lead to a transition between the brittle and ductile layer, called the brittle-ductile transition (BDT). The thickness of the elastic layer is of utmost importance in many models of surface evolution. The brittle-elastic-ductile structure in the icy bodies can be most easily modeled as a purely elastic layer over an inviscid fluid (zero viscosity) interior (e.g. *McNutt*, 1984; *Collins et al.*, 2009). The thickness of this layer can then be used to better constrain the temperature gradient within a shell (*Golombek and Banerdt*, 1986). Most estimates of the elastic thickness T_e are determined by surface topography when a load is bending the surface. While in reality even very cold surface ice can

relax over long timescales (i.e., behave viscously), most models of the ice shells make the simplifying assumption that surface deformation in response to tectonic stresses and surface loading is elastic.

CHAPTER III

The role of structural and environmental triggers inferred from an Antarctic-wide survey of ice shelf rift propagation

3.1 Introduction

The Antarctic Ice Sheet is surrounded by platforms of floating ice called ice shelves, which are freely floating seaward extensions of the grounded ice sheet. Ice shelves play a crucial role in the overall mass balance of the Antarctic Ice Sheet because they are the sites of the majority of the mass loss from the ice sheet to the Southern Ocean (*Rignot et al.*, 2008). Although mass lost from ice shelves does not directly contribute to sea level rise, observation show that thinning, retreat, or demise of ice shelves is linked to increased discharge of grounded ice (*Scambos et al.*, 2004; *Rignot et al.*, 2004; *Pritchard et al.*, 2012), providing an indirect link between ice sheet stability and sea level rise.

Mass loss from ice shelves occurs primarily through the processes of iceberg calving and basal melting. Of these two processes, iceberg calving remains the least well understood. This is partly due to the fact that calving events from Antarctic ice shelves occur sporadically with long (decades or longer) recurrence intervals between major calving events (*Lazzara et al.*, 1999; *Fricker et al.*, 2002). Moreover, observations over

the past decade show that ice shelves exhibit a spectrum of calving behaviors. At one extreme end of the calving style spectrum, calving occurs in abrupt ice shelf disintegration events, for example those events observed in both the Larsen A and Larsen B ice shelves following a series of abnormally warm summers (*Scambos et al.*, 2003). Not only were these disintegrations surprising in terms of their size, but also in the short time over which they occurred; Larsen B Ice Shelf collapsed over the course of three weeks (*Scambos et al.*, 2003; *Glasser and Scambos*, 2008) and has been related to the abundance of surface melt associated with the approximately 3°C increase in temperature at the Antarctic Peninsula over the last half of the century (*Steffen et al.*, 2008). Recent observations on Larsen C ice shelf have also pointed to the potential role of wide basal crevasses in destabilizing the ice shelf (*Luckman et al.*, 2012; *McGrath et al.*, 2012). On the other end of the spectrum, the larger ice shelves (Ross, Filchner-Ronne, and Amery ice shelves) are located in a colder climate, farther south than the Antarctic Peninsula, and have not experienced comparable surface warming nor are they currently showing any signs of imminent peninsular-style disintegration.

In this study we investigated the process that precedes iceberg calving, rift propagation. Ice shelf rifts are fractures in the ice that have completely severed the ice thickness; alternately, crevasses, which may initiate from the base or surface of the ice shelf, are fractures that have not fully severed the ice thickness. Rifts can propagate for decades before becoming the detachment boundaries of icebergs. Previous studies have found conflicting evidence on what variables drive rift propagation, with some studies suggesting that rift propagation is driven by the internal glaciological stress (*Joughin and MacAyeal*, 2005; *Bassis et al.*, 2005, 2008) whereas other studies have proposed that the timing of iceberg calving events may be related to the arrival of pulses of ocean swell (*MacAyeal et al.*, 2006; *Bromirski et al.*, 2010) or even the arrival of tsunamis (*Brunt et al.*, 2011). Previous studies have also noted that rifts tend to arrest at suture zones between ice streams (*Hulbe et al.*, 2010; *Glasser et al.*,

2009; *McGrath et al.*, 2012) with some speculation that marine ice filling these suture zones may form a barrier to rift propagation (*Holland et al.*, 2010; *McGrath et al.*, 2012). However, these studies have been based on a small sample of ice shelves and it is not clear if these observations are universal or specific to individual ice shelves and glaciological settings.

To address this, we conducted an Antarctic-wide survey of ice shelf rift propagation rates for the decade 2002-2012. We tracked 78 rifts within 30 km of the calving fronts of 13 ice shelves. Ice shelves were selected to provide broad geographical coverage around the continent and to represent a variety of physical and environmental settings; their sizes ranged from the largest ice shelves (e.g., the Ross and Filchner-Ronne ice shelves) to smaller ice shelves (e.g. the Wilkins and West ice shelves). We used the dataset to test hypotheses of the effects of physical setting and external variables on rift propagation and arrest.

3.2 Data and Methods

3.2.1 Satellite imagery and image processing

We used images from two different sensors on two separate spacecraft to maximize temporal sampling: the Multi-angle Imaging SpectroRadiometer (MISR; pixel size 275 m) on NASA's Terra satellite and the Moderate resolution Imaging Spectroradiometer (MODIS; pixel size 250 m) on both the Terra and Aqua satellites. We searched through all available browse images of the ice shelf fronts between January 2002 and March 2012 to determine suitable images, and selected only those that had a unobscured view of the ice front, i.e., only during cloud-free, summer days (September to April).

We used visible channel MODIS imagery, which was available online from the National Snow and Ice Data Center (NSIDC) and required no additional processing

(*Scambos et al.*, 1996). For MISR, we generated false-color composites using the CF, AN, and CA bands with the publicly available MISRView software. This allowed better detection of the rifts in the MISR images; by using this combination of bands from cameras looking at different angles, color acts as a proxy for angular reflectance variations which are related to surface texture, and enhances the rifts (*Fricker et al.*, 2005). For each MODIS and MISR image, we performed contrast-stretching, toning and brightening to enhance the visibility of the rifts and increase our ability to differentiate between the rift and ice shelf (*Fricker et al.*, 2005). We analyzed about 60 images for each of the 78 rifts over the decade, for a total of approximately 4680 images.

3.2.2 Rift length measurement

To estimate the propagation rates for each study rift, we measured the length of each rift in every clear image (Fig. 3.1). We did not consider rift widening. For "front initiated" rifts (i.e., initiated from the calving front and propagating inward into the ice shelf) we measured the distance from the upstream rift wall edge to the rift tip. For rifts originating from an interior point or a triple junction we measured from tip-to-tip or from the center of the triple junction to the rift tips. We define the "rift tip" as the final point at which a rift pixel is discernible from the background; the true rift tip may extend much further than we can resolve in the MODIS and MISR images if the rift becomes very narrow near its tip (i.e., narrower than a single pixel). Our estimated uncertainty in identifying this point is approximately one-pixel ($\sim$275 m for MISR, $\sim$250m for MODIS). Because we only measure distances between two points on an image, we do not require any geolocation information.

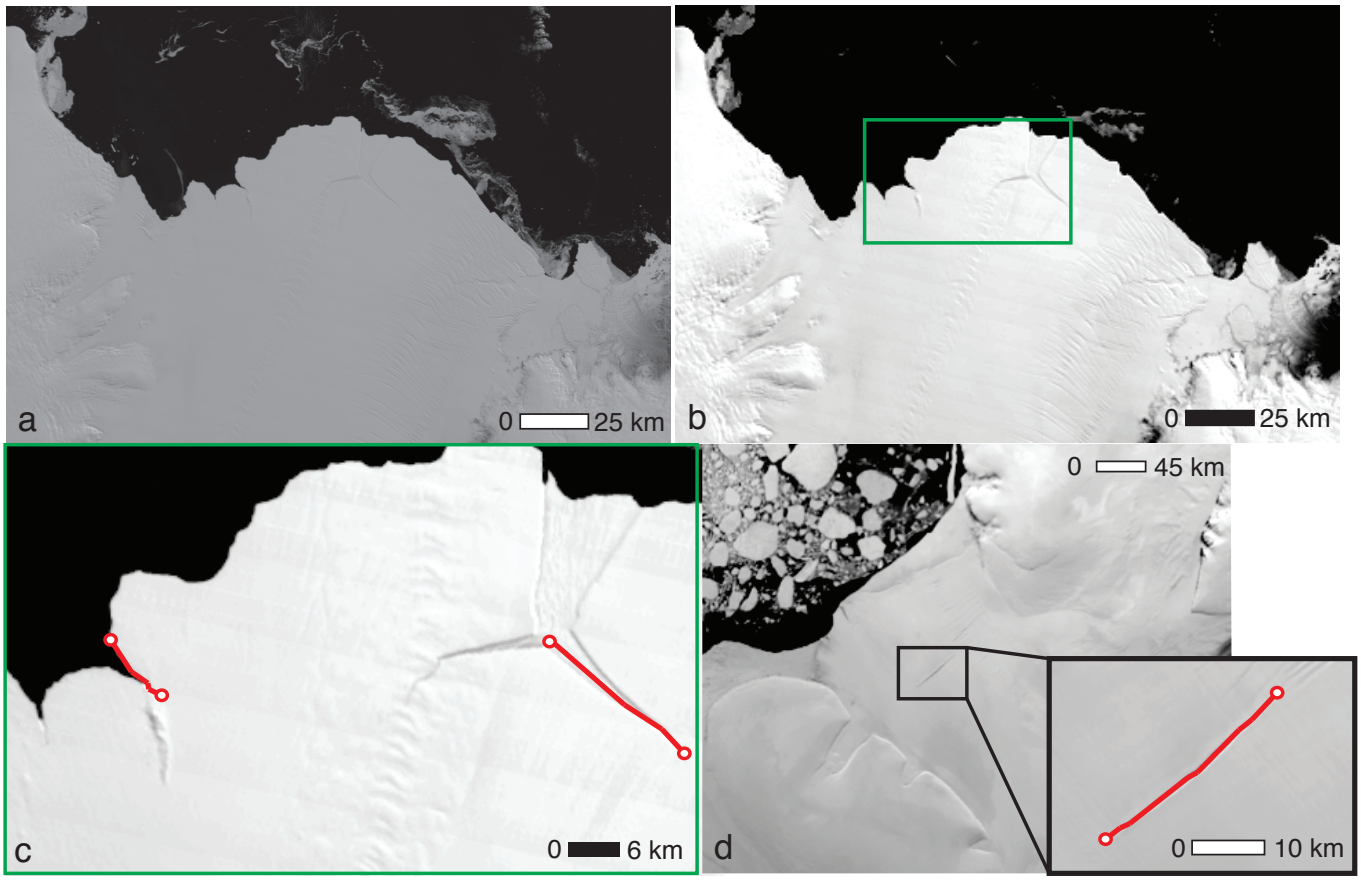

Figure 3.1: Image enhancement and methods of measuring rift length for different rift orientations. (a) Raw MODIS image of the Amery Ice Shelf from 11 February 2012. (b) Brightened and contrast-stretched version of same MODIS image. (c) Red circles denote beginning and end points for measuring rifts. Shown here is a front-initiated rift (left) and a rift initiated from a triple junction (right). Red lines denote the measured length. (d) The Fimbul Ice Shelf in a contrast-enhanced MODIS image from February 2012. Inset: Red circles denote beginning and end points of measurement for a double-ended rift.

3.3 Results

3.3.1 Propagation patterns

The distribution of rift activity type around the continent is shown in Fig. 3.2 and tabulated in Table 1. These observations can be categorized into two general behavioral categories, characterized by the recurrence interval between rift propagation events. These categories are defined as: (1) *dormant rifts*, defined as rifts that did not propagate over the decade (i.e., propagation is less than ∼500 m over the decade); (2) *active rifts*, defined as rifts that lengthened by more than ∼500 m over the decade. Active rifts were further subdivided into: (i) *continuously active rifts*, where the recurrence intervals between propagation events was comparable to or smaller than the repeat pass time of image acquisition, giving the appearance of continuous propagation; (ii) *intermittently active rifts*, which appeared to propagate continuously for two or more years and then became dormant, and; (iii) *sudden burst active rifts*, which exhibited propagation events that were larger than ∼500 m after two or more years of dormancy.

Of the 78 rifts monitored, 43 rifts (55%) showed no change in length and so qualified as dormant, making dormancy the primary behavior observed. Of the remaining 35 active rifts, seven were continuously active: five on the Amery Ice Shelf, one on the Fimbul Ice Shelf, and one on the Filchner Ice Shelf (supplementary Figs. S1, S2, and S3). All of these rifts are front-initiated. We found that the rifts on Amery Ice Shelf are more active compared to rifts on any of the other ice shelves. Another eight rifts qualified as "intermittently active", propagating for at least two years before arresting. Of these eight intermittently-active rifts, five were front-initiated. Two more of these rifts were double-ended upstream rifts (one each on West Ice Shelf and on Ross Ice Shelf) that initiated in the interior of the ice shelf, away from the margins and lengthen from both rift tips (e.g., supplementary Fig. S3, panel 2). The eighth

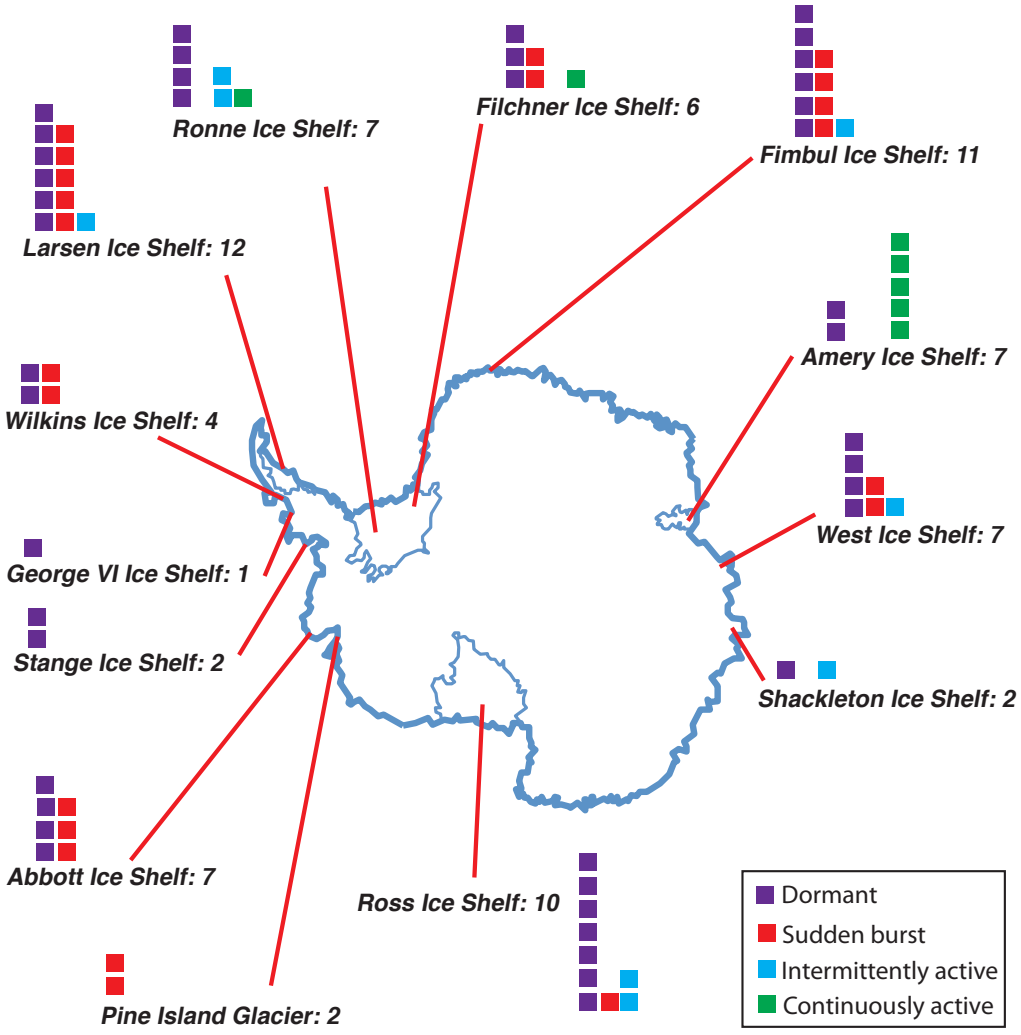

Figure 3.2: Ice shelf locations and categories of rift propagation observed. Each block denotes a rift and the color of the block denotes the type of rift activity observed (see legend).

intermittently active rift was in the remnant Larsen B Ice Shelf and initiated from the Jason Peninsula (supplementary Fig. S5). The remaining 20 active rifts qualified as sudden burst types.

3.3.2 Temporal patterns of rift propagation

We examined temporal patterns in propagation for the 35 rifts that were active over some portion of the decade. Although there is a data gap during the Austral winter, for most rifts, the length of the rift at the end of each Austral summer was typically within one pixel of its length at the beginning of the following summer, indicating that rift propagation primarily occurs during the summer (Table 1; *Fricker et al.* (2005)). There were three exceptions to this; we observed wintertime propagation for one rift in the Ronne Ice Shelf, one in the West Ice Shelf, and one in the Ross Ice Shelf (supplementary Fig. S12). The latter two rifts were both double-ended rifts, that propagated at both ends.

Temporal patterns of rift propagation were highly variable over the decade with little evidence of an Antarctic-wide increase in rift propagation activity (Fig. 3.3). Fluctuations in rift propagation rates were, however, large and over the limited duration of our study we cannot discount a longer-term change in rift propagation rates that is masked by the shorter-term variability. Variability in propagation within a given ice shelf (and sometimes within a single rift) can be as large as the variability in rift propagation observed in different ice shelves.

3.4 Discussion

The majority of rifts that we observed (43 of 78) were dormant for the entire decade. Many of these rifts initiated far upstream of the calving front and have been advecting downstream for decades with the main ice shelf flow (e.g. *Hulbe et al.*, 2010). The fact that the majority of upstream rifts were dormant suggests that once

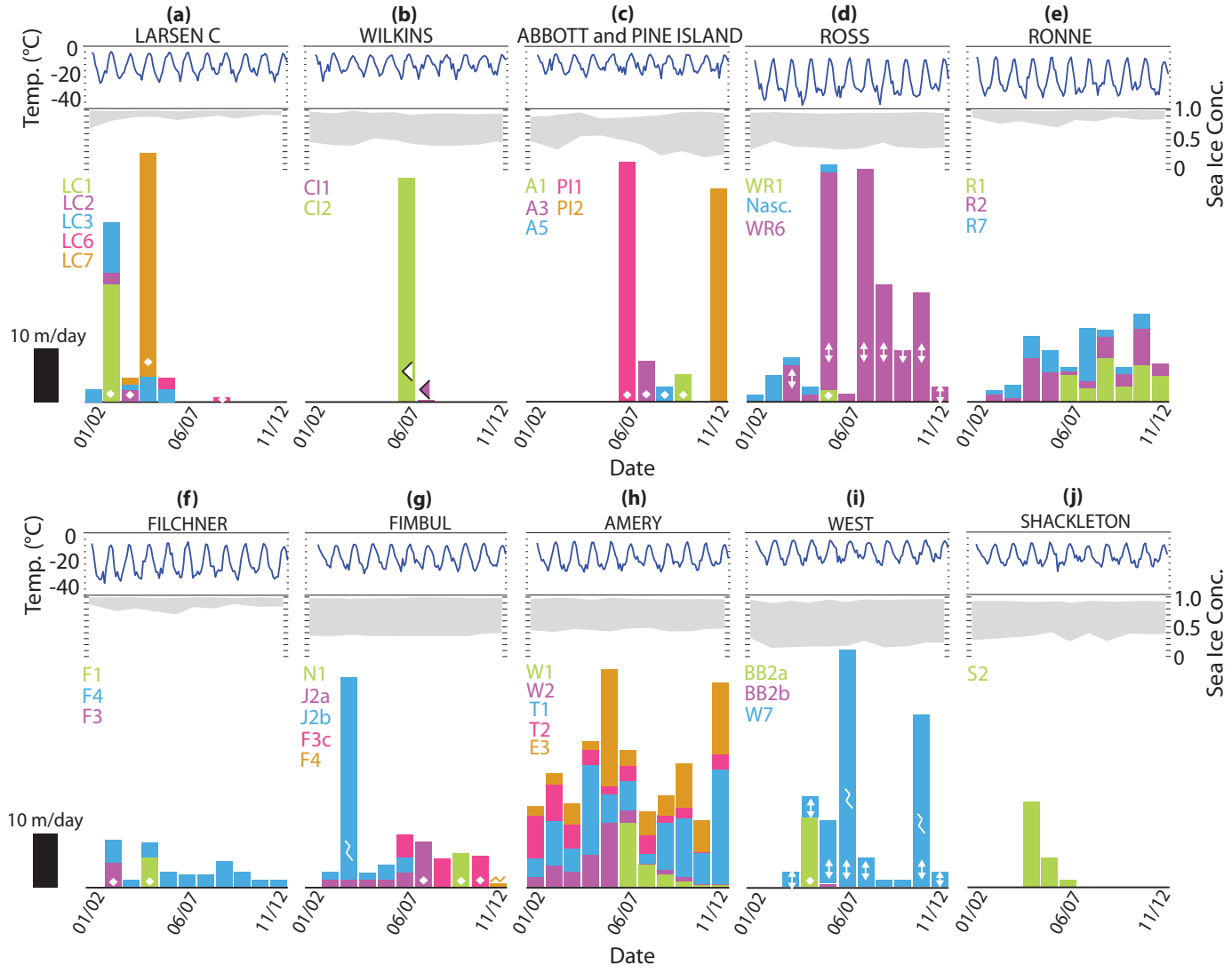

Figure 3.3: Each panel shows atmospheric temperature, the monthly range of sea ice concentration from maxima and minima and rift propagation rates for each ice shelf. Top: Monthly mean temperatures for each ice shelf over the decade, from ERA interim reanalysis data. Middle: Gray shaded regions are maximum and minimum annual sea ice extents in front of each ice shelf from passive microwave measurements. Bottom: The length of each bar represents the annual propagation rate with bars color coded to label the different rifts in ice shelves (supplementary Figs. S1-S10). White arrows signify rifts with two actively propagating rift tips. White diamonds signify calving events. White zig-zag signifies rifts propagating in a crevasse field. Left-triangles signify a collapse event.

these rifts become inactive, they are not easily re-activated. This is supported by observations of the crevasse field at the northeastern front of the Amery Ice Shelf (supplementary Fig. S1). These crevasses advect towards the front, but do not significantly change length once they have initiated upstream. In contrast, the most active rifts in our study were all front-initiated, implying that iceberg calving may be more tightly controlled by near calving-front fracture processes than reactivation of dormant rifts that initiated upstream of the calving front.

We observed large variability in rift propagation in those rifts that were active. We first consider whether or not this variability is related to fluctuation in environmental setting, though our observations do not display an immediately-obvious geographical trend. Alternatively, we speculate that variability in rift propagation is controlled by mechanical heterogeneity, i.e., structural changes such as crevasses or changes in ice type and ice properties. Such changes over a sub-kilometer scale could explain the variability in propagation rate of a single rift over time and, in the case of more than one active rift on a given shelf, in propagation rate disparity between rifts. We further examine these possible controls on rift propagation in the sections that follow.

3.4.1 Role of environmental forcing

3.4.1.1 Atmospheric temperatures and ocean swell

Previous studies have linked both warming atmospheric temperatures and mechanical forcing from the ocean to ice shelf disintegration (e.g. *Mueller et al.*, 2008), motivating us to investigate whether any of the variability in rift propagation regimes is correlated with either (i) atmospheric temperature fluctuation or (ii) changes in sea ice concentration. We use sea ice as a proxy for mechanical-ocean forcing because its presence will damp ocean waves. Unfortunately, the long wavelengths associated with infra-gravity waves (e.g. *Bromirski et al.*, 2010) will not be efficiently damped by sea ice and their influence is not considered in this study. For atmospheric temperature

we used monthly means of atmospheric reanalysis (ERA-Interim) 2-meter air temperature data, at a spatial resolution of 1.5°, obtained from the European Centre for Medium-Range Weather Forecasts Data Server (ECMWF); for sea-ice concentration we used monthly sea ice concentrations obtained from Nimbus-7 SMMR and DMSP SSM/I-SSMIS passive microwave data archived at the NSIDC.

Observed propagation rates displayed no obvious correlation with atmospheric temperature (Fig. 3.3). Although warmer temperatures occur in more northern regions, ice shelves in those locations (e.g., the Larsen C, Wilkins, and Abbott ice shelves) do not show a significantly higher level of activity than colder ice shelves (e.g. the Ross and Filchner-Ronne ice shelves). We see little evidence that warmer ice shelves have more active rift systems than colder ice shelves. We do not see a clear signal of an atmospheric temperature threshold, above which one or more rifts in a given ice shelf is prone to propagation. We did, however, note occasional correlations between summer rift activity and temperature of the previous winter, but these correlations were opposite to our expectations. Contrary to expectation, warmer winter seasons did not lead to increased activity, e.g., in winter 2007, the Amery, West, and Shackleton ice shelves experienced warmer-than-average winters, but active rifts in all three ice shelves showed a decreased propagation rate (the Amery and West ice shelves) or complete arrest (the Shackleton Ice Shelf) during the following Austral summer season. Similarly, three rifts in the Amery Ice Shelf (rifts W2, T1, and T2 in supplementary Fig. S2) propagated over the wintertime in 2005, during a relatively cold winter when compared to average winter temperatures of other years.

Fig. 3.3 shows the range of sea ice concentration observed over the decade using monthly maxima and minima values of sea ice concentration. We do not find a correlation between sea ice concentration and rift activity. For instance, the ice shelves that are adjacent to the Weddell Sea, e.g., the Larsen C, Ronne, and Filchner

ice shelves, experience much less variability in sea ice concentration, since sea ice remains abundant throughout the year. However, these ice shelves do not exhibit decreased rift activity nor do we see evidence that an increase in rift activity is correlated with abnormally low sea ice concentration at any of the ice shelves.

3.4.1.2 The effect of tsunamis

It has been previously suggested that the arrival of tsunamis may affect ice shelf rift propagation (e.g. *Brunt et al.*, 2011). However, studies based on a single observed instance of a well-correlated propagation event with a tsunami arrival are difficult to qualify as causal rather than it being simply coincidental (*Bassis et al.*, 2008). Using our large dataset, we further investigated the likelihood that tsunamis might affect rift propagation. We did observe a correlation between the arrival of tsunamis and the propagation rifts, including some rifts that had previously been dormant. All five rifts in the Amery Ice Shelf propagated between 26 December 2004 and 09 January 2005, following the 26 December 2004 tsunami that originated west of Sumatra. Six additional incidences of rift propagation events on other ice shelves occurred at the end of December 2004. These ice shelves are all exposed to the Indian Ocean and were in line with computed wave paths and in-situ buoy measurements, available from the National Oceanic and Atmospheric Administration (NOAA) Center for Tsunami Research. The only exception to this is the Ronne Ice Shelf, which did not experience any rift propagation events following the tsunami. Moreover, we observed additional instances of large rift propagation events in both the Amery Ice Shelf and other ice shelves following the arrival of other tsunamis originating in both the Indian and Pacific Oceans (Fig. 3.4). "Large propagation events" are defined here as events with a propagation rate above the interquartile range of the data. To determine if this connection is statistically significant or merely coincidence, we used a chi-squared test (e.g. *Mighell*, 2000) to determine the probability that the coincidence between

these events is random and found that the correlation between the arrival of the tsunami and the timing of large bursts of propagation is statistically significant at the 90% confidence level. Intriguingly, all of the instances in which we observed rift propagation following the arrival of a tsunami occurred in front-initiated rifts. These rifts are open to the ocean and we hypothesize that fluctuations in wave height near the calving front can be channeled into the rift and this wave field creates a large pressure concentration as the waves converge near the rift tip.

3.4.2 Role of mechanical forcing controls on rift propagation

3.4.2.1 Suture zones

We observed large variability in rift propagation in those rifts that were active, but found little evidence that ice-shelf-scale environmental forcing controls this variability. This leads us to speculate that variability in rift propagation is controlled by mechanical heterogeneity, i.e., structural changes such as crevasses or changes in ice type and ice properties. It has been suggested previously that suture zones may serve as barriers to the propagation of rifts, as dormant rifts are often observed to coincide with suture zones between ice from adjacent ice streams (*Hulbe et al.*, 2010; *McGrath et al.*, 2012). Table 1 shows that roughly one-quarter of rifts that were dormant or intermittently active had propagated into a known suture zone in the shelf; however, this behavior is not universal. We observed at least two rifts propagate through nearby suture zones at an increased rate instead of arresting. For example, rift T1 in the Amery Ice Shelf (supplementary Fig. S1) propagated through a suture zone. Rather than slowing down, it sped up as it propagated through the suture zone. Likewise, we observed rifts R1 and R2 on the Ronne Ice Shelf (supplementary Fig. S4) propagate through suture zones prior to their arrest a year to two years later.

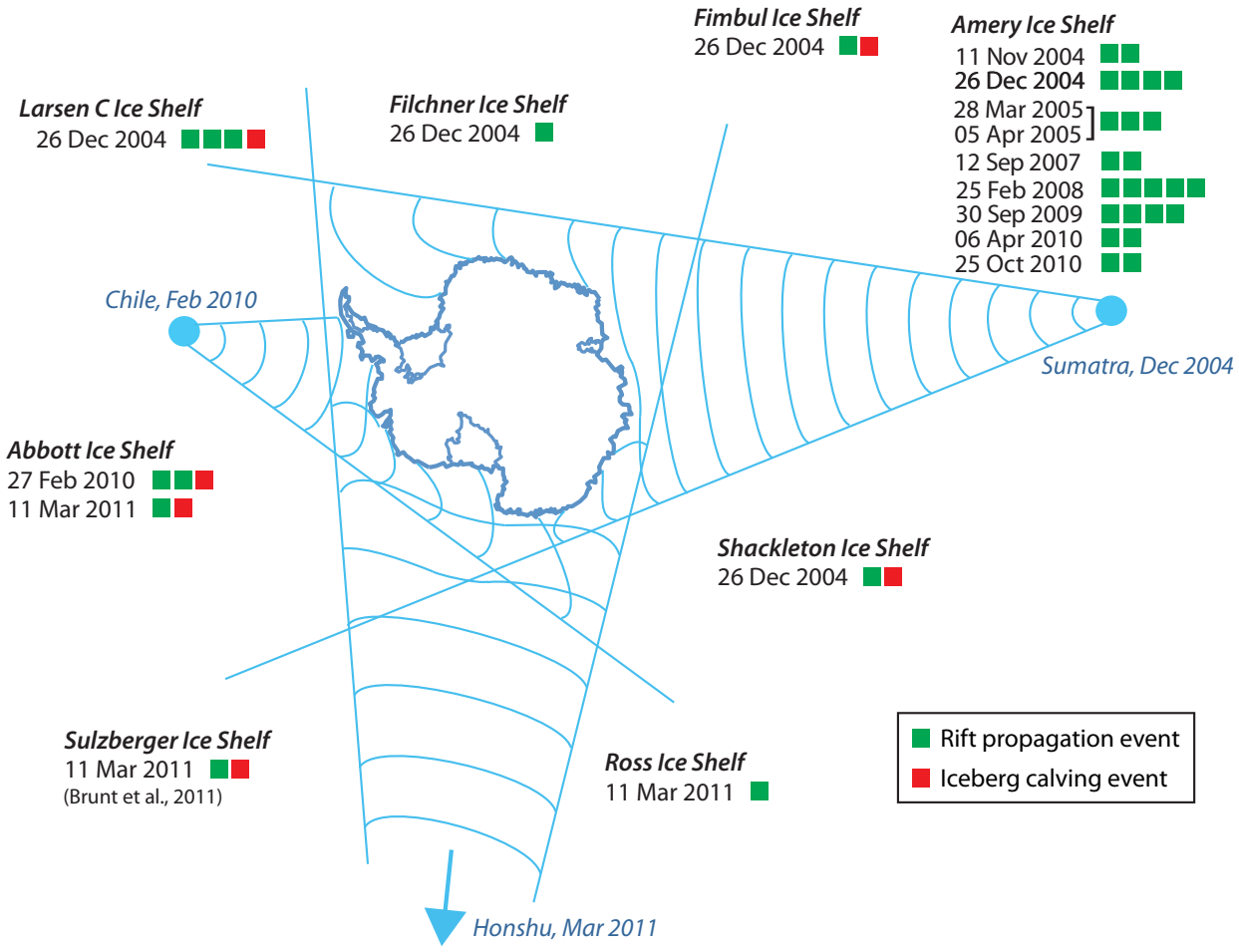

Figure 3.4: Examples of rifts that exhibited propagation events following the arrival of a tsunami. Each block indicates a rift that propagated following the arrival of a tsunami. The color of the block denotes whether the rift propagation event was also associated with an iceberg calving event. Rift propagation was observed in the rifts that are exposed to the specific wave path of a given tsunami. Wave paths associated with tsunamis that originated near Sumatra, Chile and Japan are sketched schematically (NOAA Center for Tsunami Research).

3.4.2.2 Marine ice

Another possible factor in the variability in rift propagation may be the existence of marine ice, which may underlie suture zones and cause a variance in ice properties, leading to mechanical heterogeneities associated with different ice types within the ice shelf (e.g. *Fricker et al.*, 2001; *Craven et al.*, 2009; *Holland et al.*, 2010; *Jansen et al.*, 2010). Unfortunately, we have insufficient observations of marine ice distributions at sub-kilometer scale to be able to more conclusively link observed variability in rift propagation rate to the presence of marine ice.

3.4.2.3 The effect of crevasses and interaction between rifts

We observed several large propagation events that coincided with the intersection of a rift with a crevasse, leading us to suggest that crevasses can serve as conduits for sudden bursts of rift propagation (e.g. *Heeszel et al.*, submitted). Alternatively, crevasses that are not optimally oriented may instead hinder rift propagation. For example, when a rift intercepts a crevasse oriented perpendicular or at an angle to the rift, additional stress buildup may be required to either propagate along the non-optimally oriented crevasse or for the rift to break through to the other side of the crevasse and continue propagating. However, once sufficient stress accumulates, the rift may propagate rapidly in a sudden burst and change direction. An example of this behavior occurs in rift E3 on the Amery Ice Shelf (supplementary Fig. S1) where the rift propagates in a zig-zag pattern, following the imprint of crevasses in the area. In total, ten of the studied rifts were located in crevasse fields, and of these only three were inactive (three on the West Ice Shelf, supplementary Fig. S10). The observed influence of crevasses on rift propagation leads us to suggest that interaction between rifts and crevasses plays an important role in modulating likelihood of an episodic burst of propagation and controlling the average rift propagation rate. Moreover, although surface crevasses are most easily identified in satellite imagery, recent ob-

servations indicate that very wide basal crevasses are often present within ice shelves and may also influence the propagation of ice shelf rifts, but have more subtle surface expressions not as readily apparent in MODIS imagery (*McGrath et al.*, 2012).

3.5 Conclusions

We have generated an observational record of Antarctic ice sheet-wide rift propagation over the decade 2002-2012, by observing rifts within 30 km of fronts on 13 Antarctic ice shelves. The variation in rifting behavior for the 78 rifts that we observed around the Antarctic Ice Sheet emphasizes that rifting is a complex and variable process, and reinforces that rift propagation is driven or controlled by more than one mechanism. Of the rifts we observed, we only found seven to be continuously active throughout the decade. The remaining rifts fell into one of these categories: (i) completely dormant, without observable motion over the decade, (ii) sudden burst propagation in which large jumps in length occurred after years of dormancy, and (iii) intermittently active rift propagation for at least two years before arrest. We did not find an observable correlation between rifting activity and changes in local atmospheric temperatures or sea ice concentration. However, we found that the arrival of tsunamis may trigger rift propagation, but only in those rifts that are front-initiated. We believe this is because these types of rifts are open to the ocean, leading to enhanced mechanical interaction between the rift and the ocean. This observational dataset shows that rift propagation is complex, but reinforces the hypothesis that mechanical heterogeneity within the ice shelf is an important control on rift propagation that needs to be further studied. Our dataset represents the most geographically extensive record of rift propagation to date, and provides a benchmark against which we can compare future rift activity.

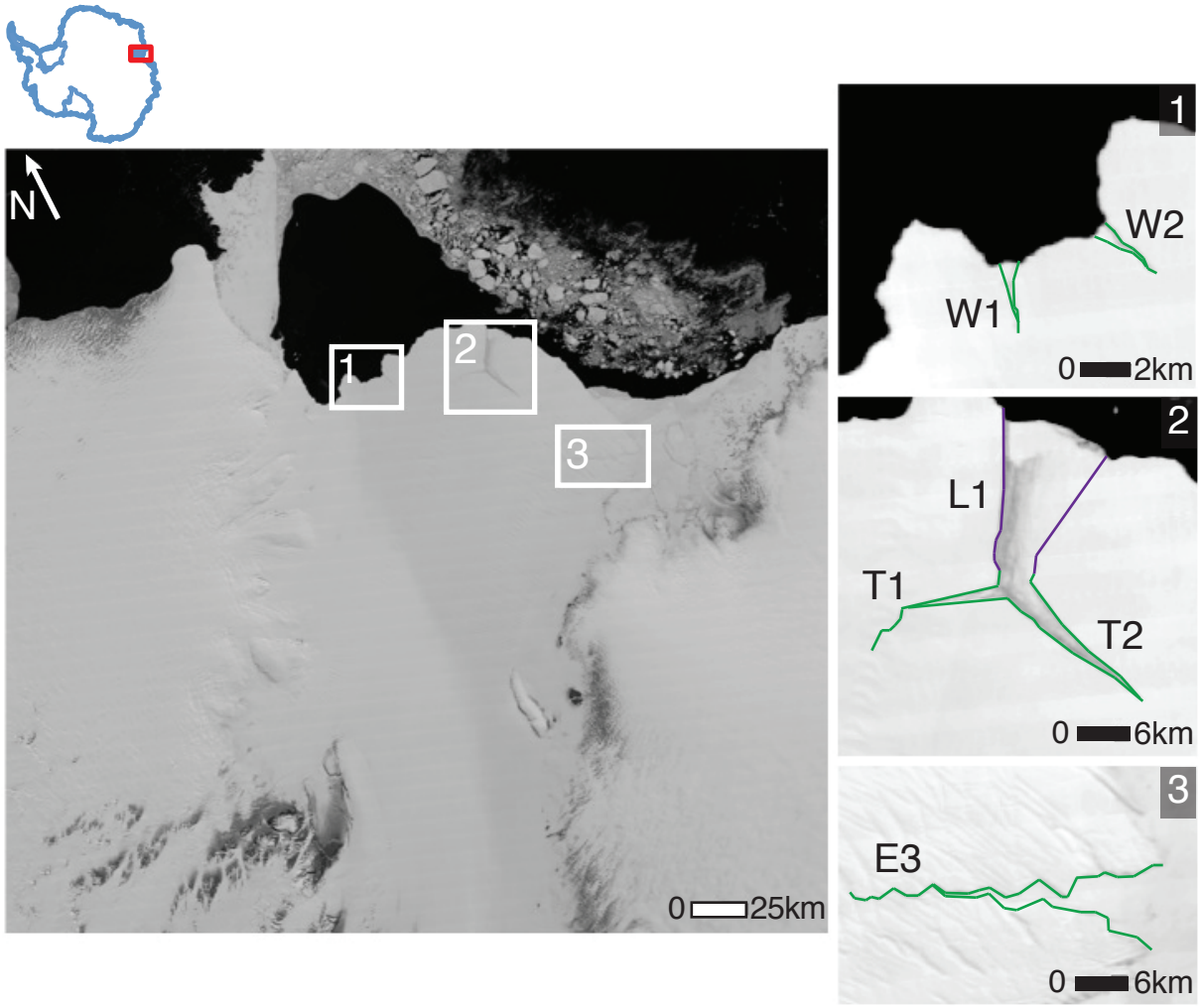

Figure 3.5: MODIS imagery from 20 December 2011 of the Amery Ice Shelf, East Antarctica (left). Zoomed views of the five rifts monitored in this study (boxes, right), color coded by activity level (legend in Fig. 1).

3.6 Supplementary Figures

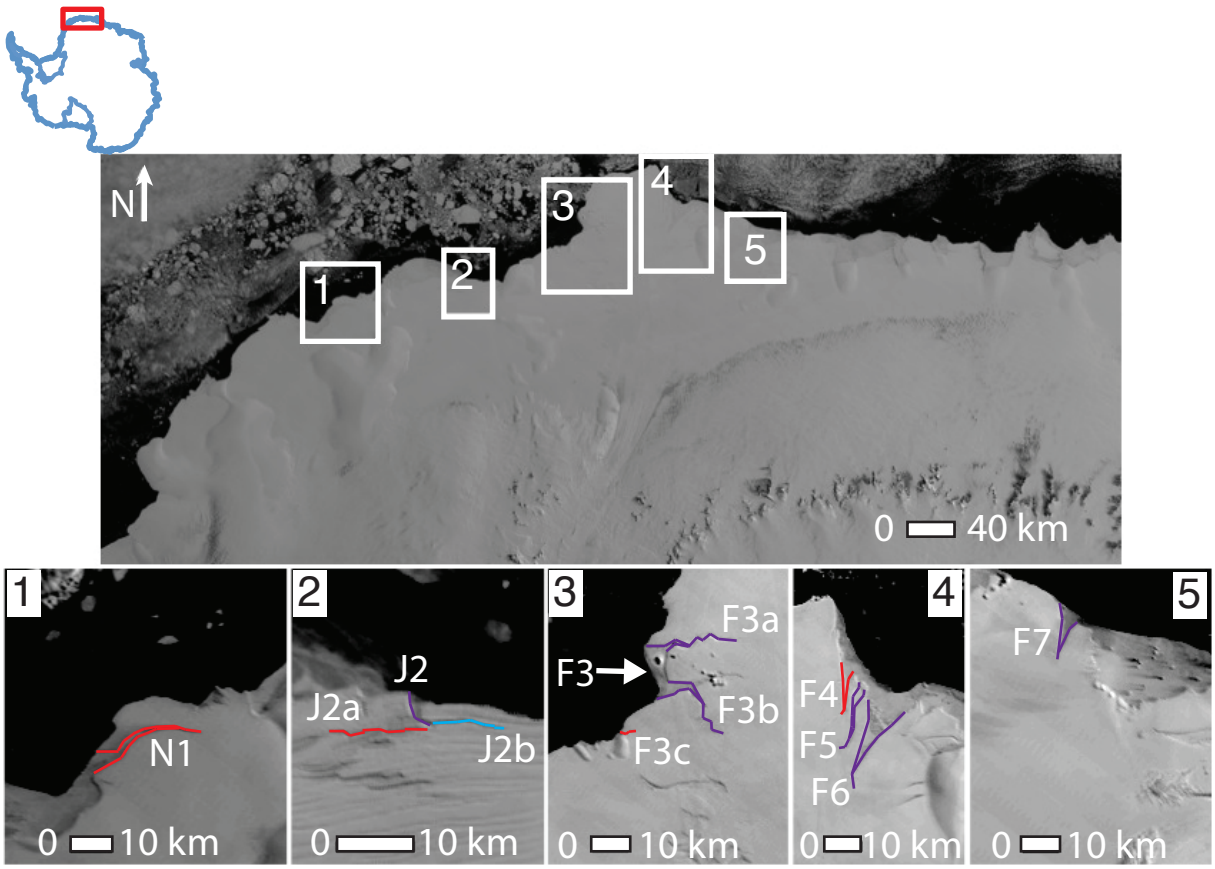

Figure 3.6: MODIS imagery of the Fimbul Ice Shelf acquired 28 November 2005 (top). Zoomed boxes (bottom) show the 11 rifts observed for this study. Rift F3 calved an iceberg prior to this study's observation period, but served as an initiation boundary for F3a and F3b.

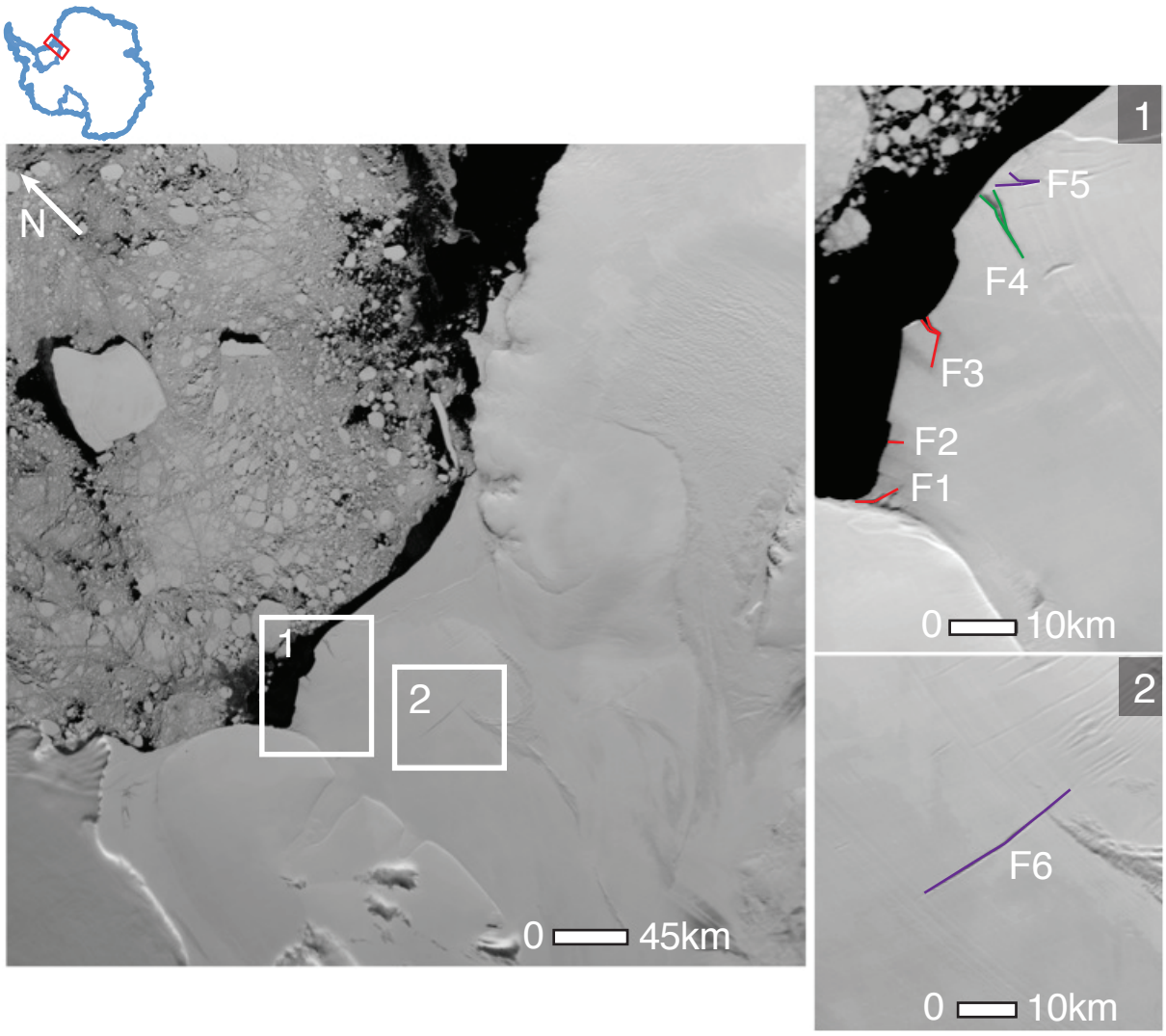

Figure 3.7: Filchner Ice Shelf (left) as imaged by MODIS acquired 13 February 2011 (left). Zoomed boxes (right) showing the six rifts observed for this study in MODIS imagery acquired 02 January 2003.

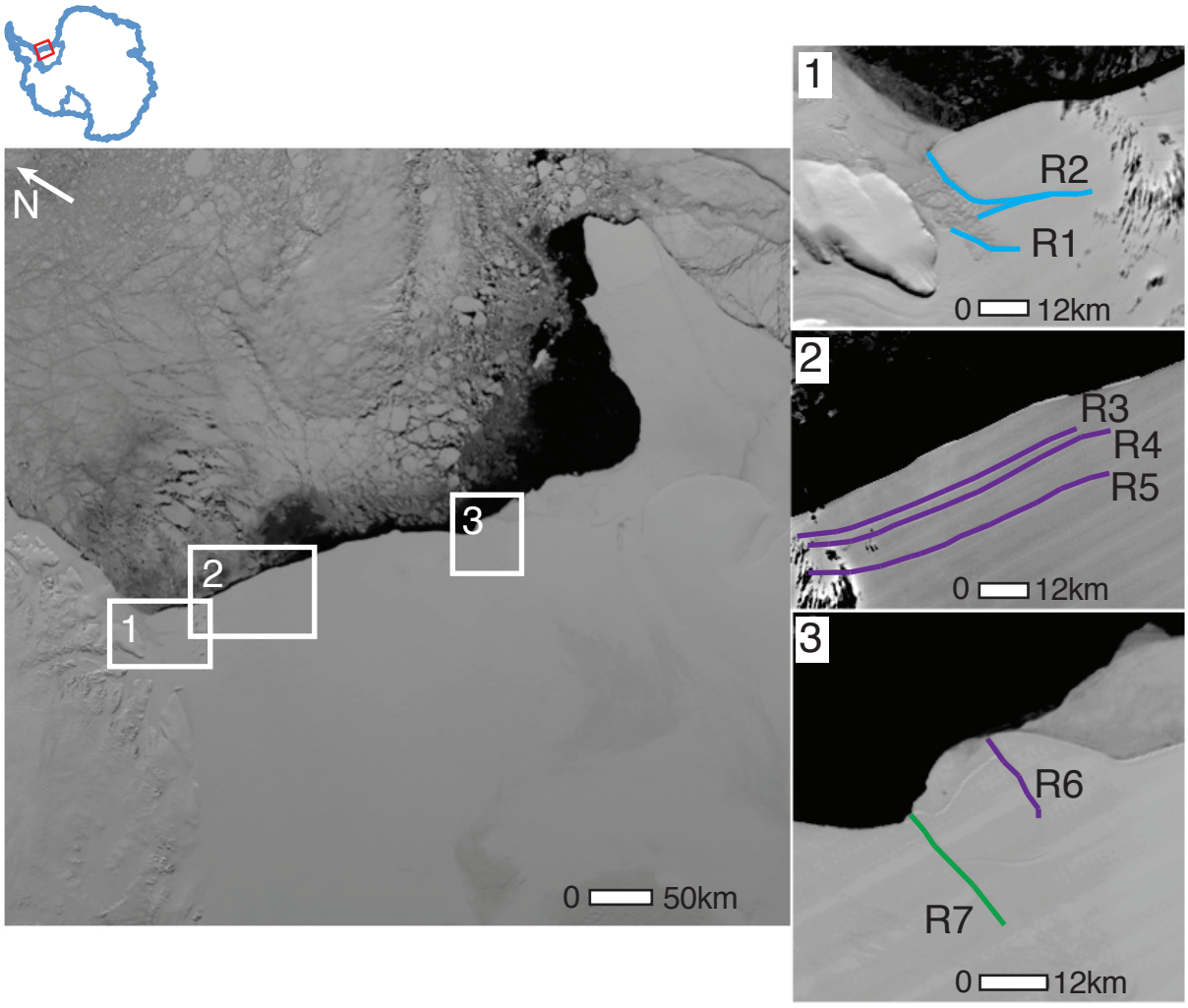

Figure 3.8: The Ronne Ice Shelf in MODIS imagery acquired 01 December 2007 (left). Zoomed boxes highlight the seven rifts observed in this study.

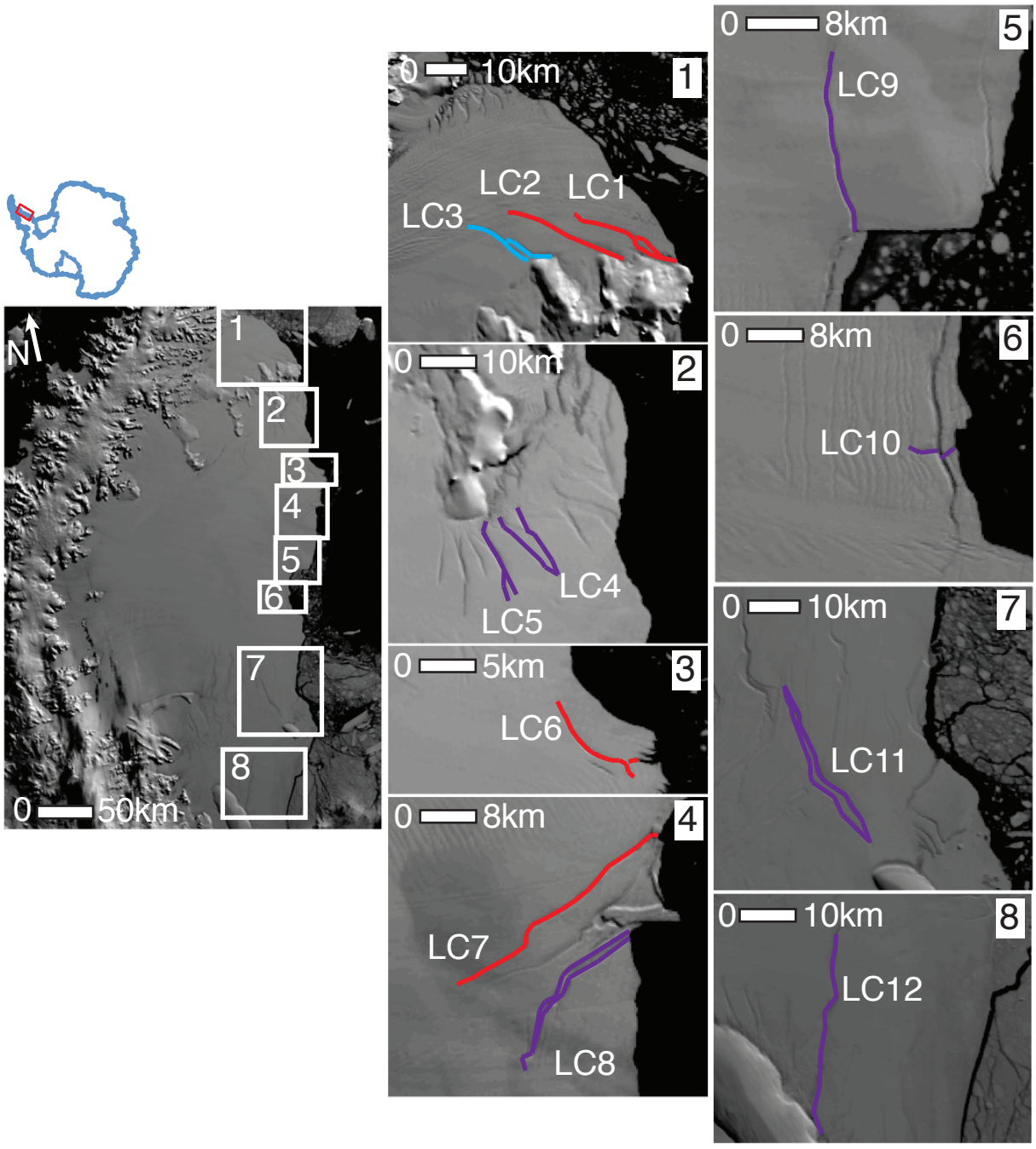

Figure 3.9: MODIS imagery from 17 March 2002 of the Larsen C Ice Shelf and remnant Larsen B Ice Shelf on the Antarctic Peninsula (right). Zoomed images of its northern rifts shown in the center column. To the right are the southern set of rifts observed in this study, a total of 11 rifts on this ice shelf.

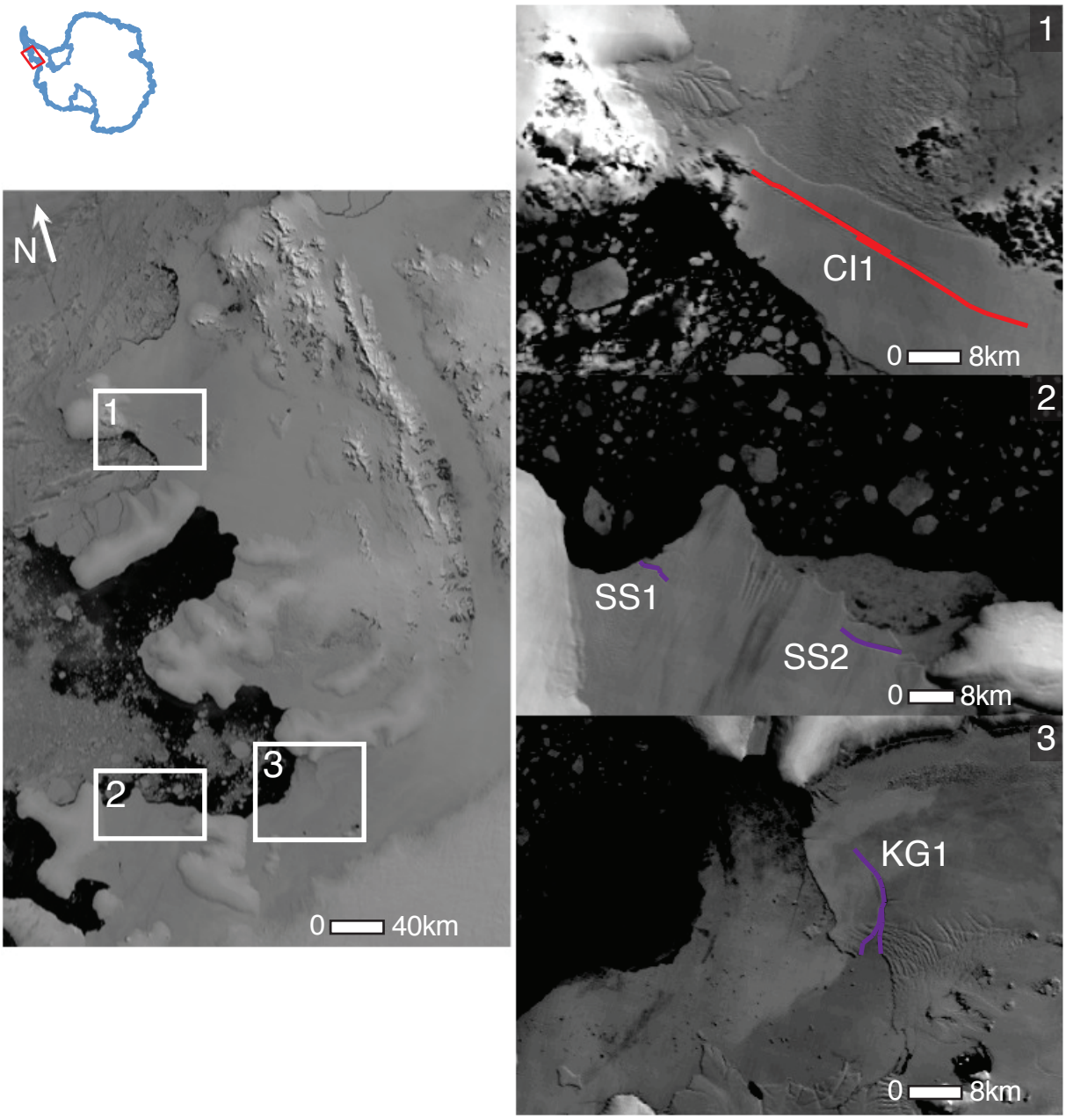

Figure 3.10: MODIS imagery from 30 December 2004 of the Wilkins, Stange, and George VI ice shelves on the Antarctic Peninsula. Zoomed images on the right exhibit the rifts observed for this study in each of the three shelves: (1) Wilkins Ice Shelf, (2) Stange Ice Shelf, and (3) George VI Ice Shelf.

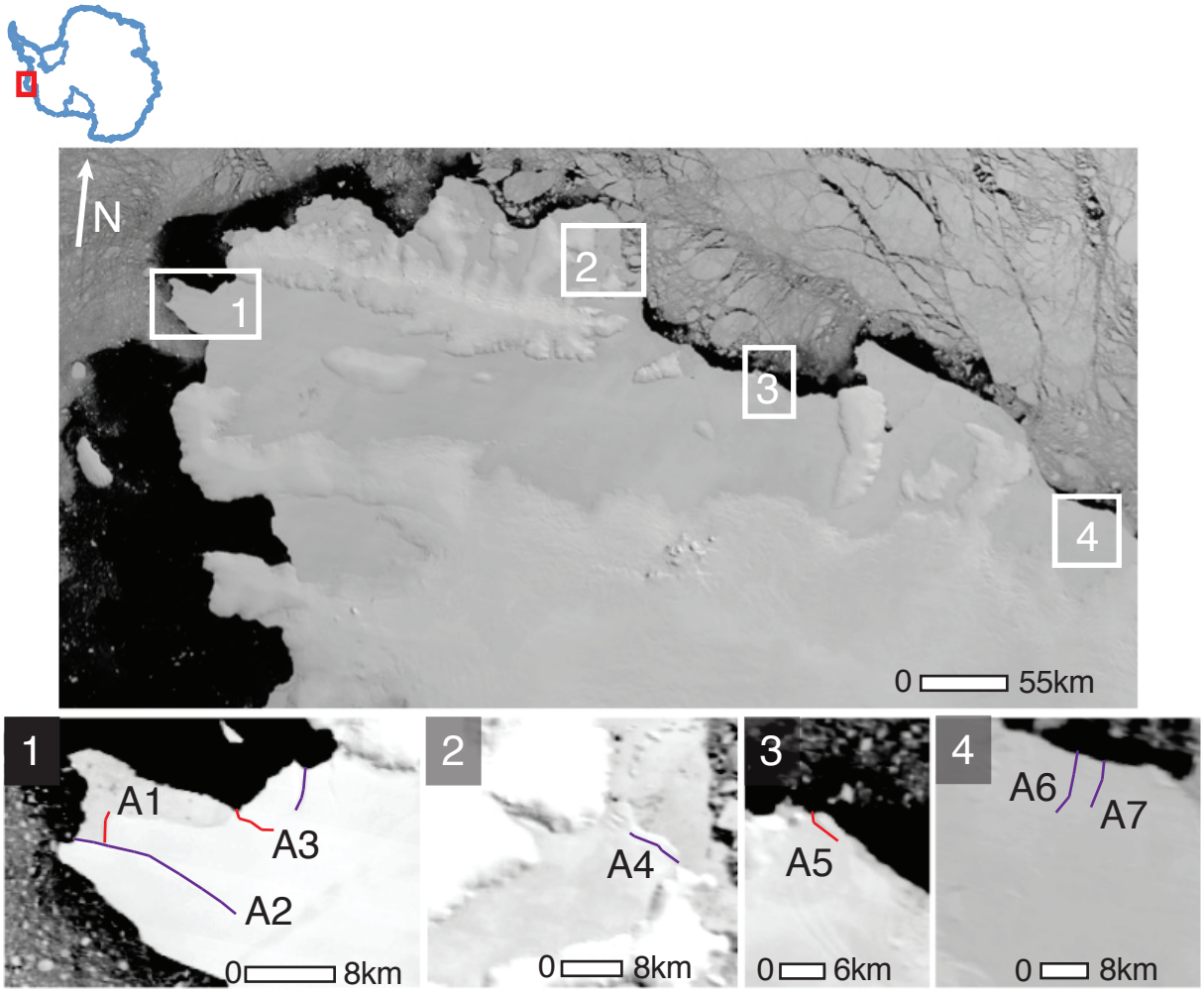

Figure 3.11: Abbott Ice Shelf in MODIS imagery acquired on 10 January 2011. Zoomed boxes (bottom) show the seven rifts observed for this study.

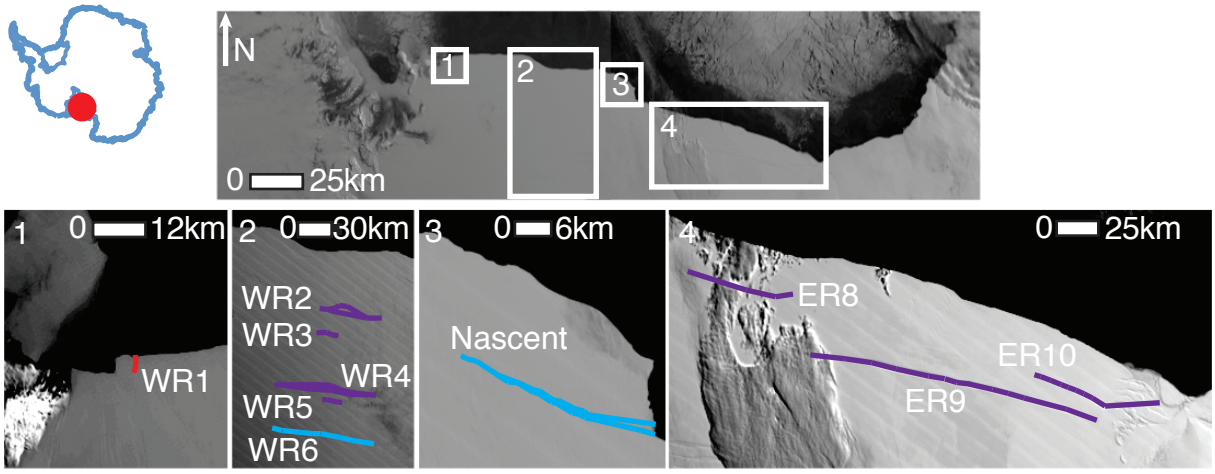

Figure 3.12: Ross Ice Shelf in MODIS imagery acquired on 16 November 2011 (top). At the bottom are zoomed images to highlight the ten rifts observed in this investigation.

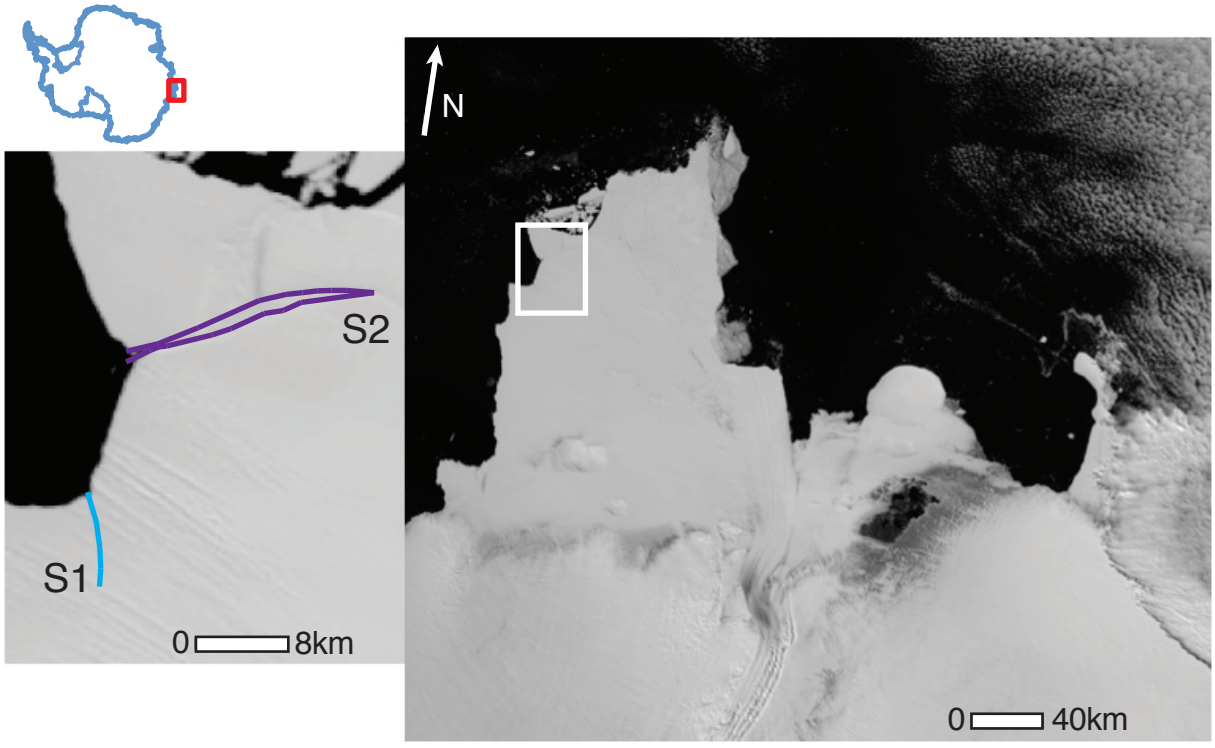

Figure 3.13: The Shackleton Ice Shelf in MODIS imagery from 20 February 2012 (right). On the left is a zoomed view of the two rifts measured in this study, stemming from a previously-calved area that spurned an iceberg immediately preceding the observing period.

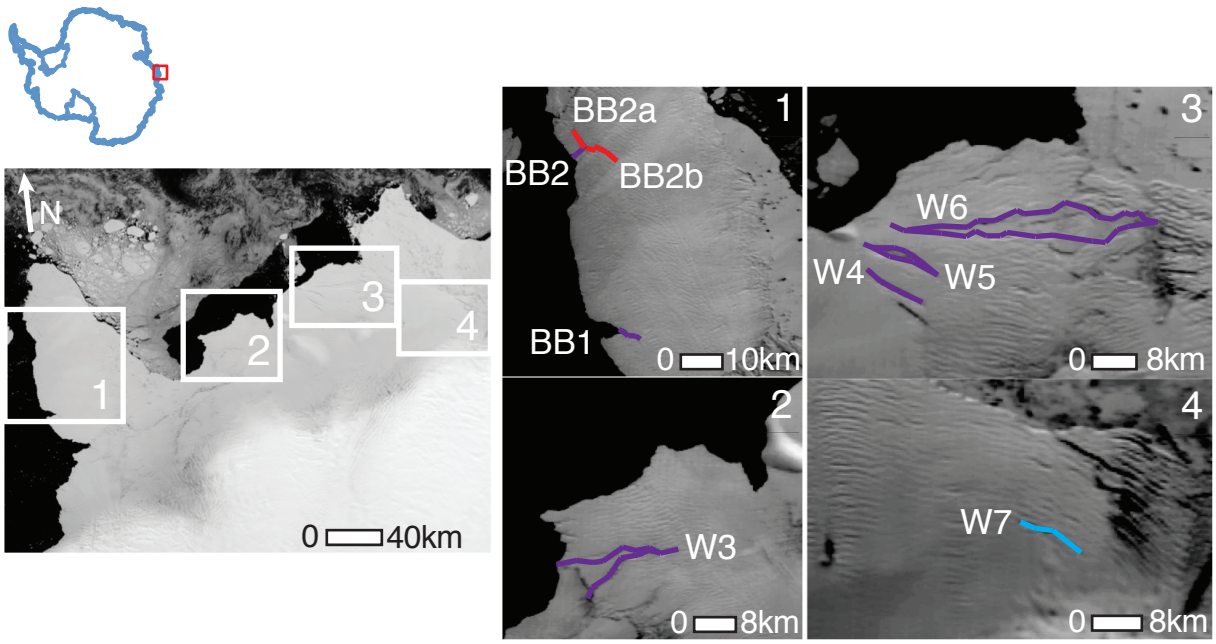

Figure 3.14: West Ice Shelf in MODIS imagery from 06 February 2004 (left). The center blocks highlight the western set of rifts observed for our study, the eastern set is shown in the zoomed images at right. Initially observing just seven rifts on the Shackleton, rift BB2 (top center) split into two new rifts (BB2a and BB2b) that we continued to observe over the decade.

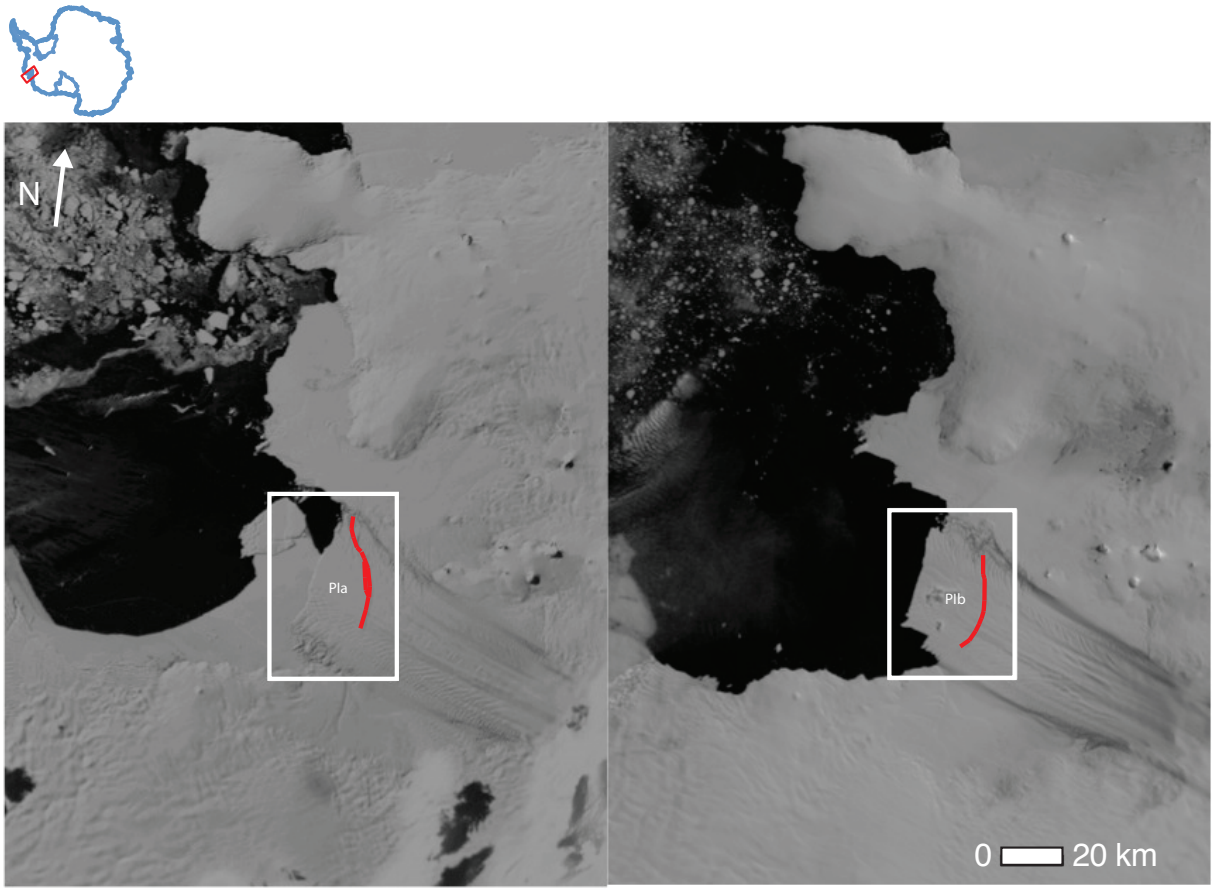

Figure 3.15: Two MODIS images of Pine Island Glacier acquired five years apart. Top: An image from 19 March 2007 shows rift PIa, which calved an iceberg in October 2007. Bottom: An image from 01 January 2012, showing that rift PIb has severed the ice approximately three-quarters across the glacier.

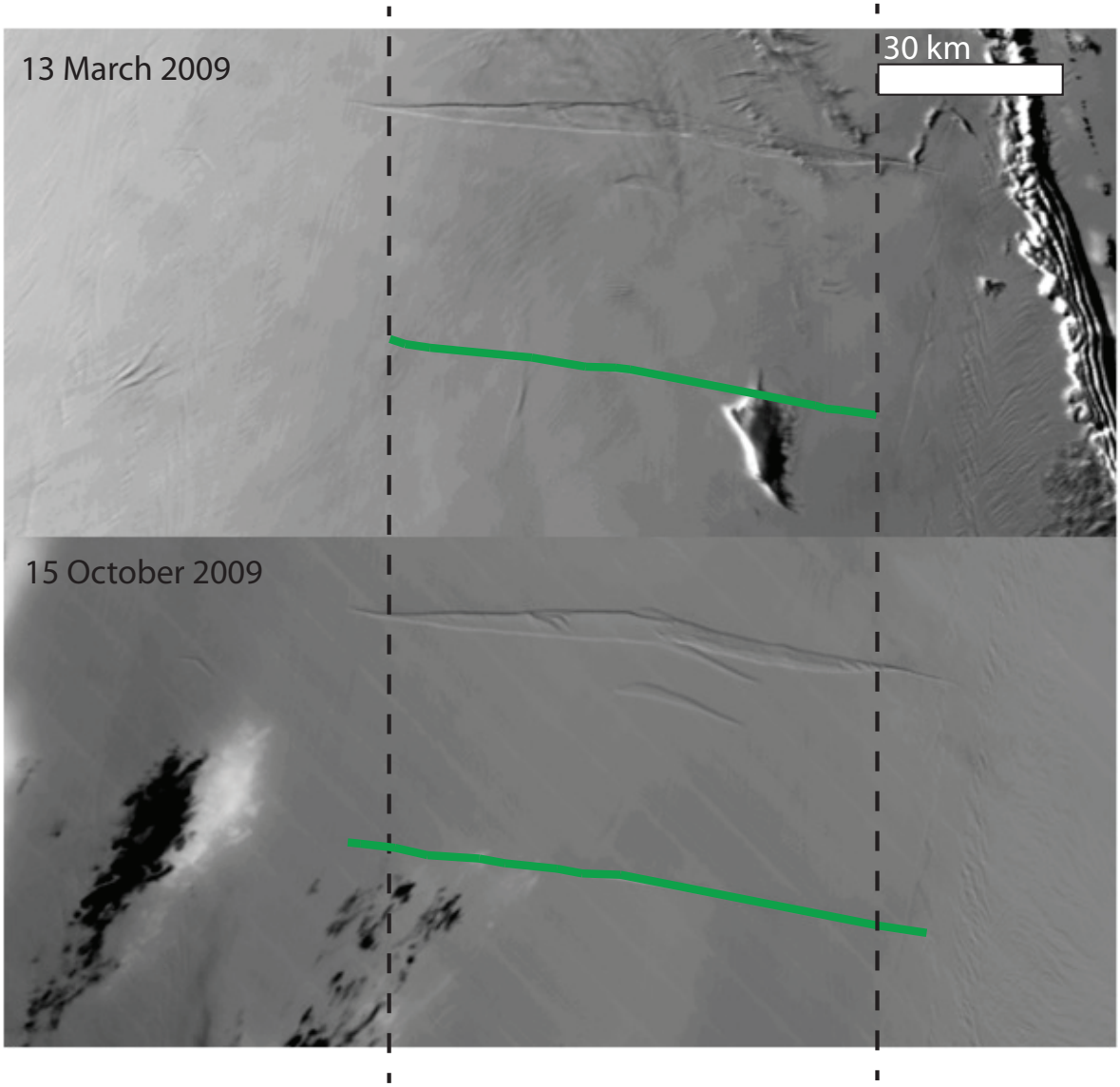

Figure 3.16: An example of wintertime propagation exhibited by rift WR6 in the Ross Ice Shelf between 13 March and 15 October 2009. Vertical dashed lines show length of rift in March 2009 (top), bottom image shows the same rift in October 2009, where it has lengthened past the length of the rift before the winter.